Available online at www.sciencedirect.com
ScienceDirect
Comput. Methods Appl. Mech. Engrg. 314 (2017) 46–70
Computer methods in applied mechanics and engineering
www.elsevier.com/locate/cma

# Computational systems mechanobiology of wound healing

Adrián Buganza Tepole

*School of Mechanical Engineering, Purdue University, West Lafayette, IN, USA*

Available online 13 May 2016

## Highlights

- We model displacements, cells, chemicals, mass fractions and microstructure geometry.
- We simulate wounds with a monolithic, fully-coupled finite element formulation.
- Linearization of residuals needs solution of a linear system at integration points.
- Wounds show contraction and contracture in an annular region surrounding the wound.
- Initially randomly distributed fibers get aligned in the wound domain.

## Abstract

Achieving perfect skin regeneration after wounding remains challenging because of the lack of fundamental understanding of the harmonious interplay among different cell types, complex cell signaling networks and mechanical feedback loops evolving in space and time during healing. Here we show a novel computational framework to simulate the healing of wounds that brings together knowledge from continuum mechanics, growth and remodeling, and systems biology regulatory networks. At the tissue scale we consider a field of displacements that satisfies linear momentum balance, and continuous fields for cells and chemical signal concentrations which obey reaction–diffusion equations. At the cell scale a set of ordinary differential equations describe the dynamics of remodeling. Our major contribution is the modeling and simulation of the coupling of cellular and chemical fields to tissue-level mechanics via local changes in fiber alignment, dispersion, collagen content, permanent area change, elastic deformation, and active contraction. Numerically, the constitutive equations for remodeling are solved at the integration points while the displacements and biological fields are solved monolithically with a finite element formulation. The method presented here is at the junction of applied mechanics and systems biology, two exciting fields that continue to approach each other as we seek to unravel the basic principles of mechanical adaptation in living materials with the aid of computational simulations.


*Keywords:* Wound healing; Skin; Remodeling; Systems biology; Finite elements

## 1. Motivation

The integrity of skin is vital for our mechanical interactions with the world. When we suffer a wound, the well defined microstructure of healthy tissue is lost, yet a remarkable sequence of events leads to tissue regeneration [1].

*E-mail address:* abuganza@purdue.edu.
*URL:* http://engineering.purdue.edu/people/abuganza.

http://dx.doi.org/10.1016/j.cma.2016.04.034

The wound healing process relies on the coordinated action of several cell types and spatiotemporal profiles of various cytokines [2]. Miraculously robust, this process is usually not optimal, and the regenerated tissue lacks the same mechanical capabilities of the intact dermis [3]. A counterexample is found in fetal wounds, which heal perfectly [4]. After we are born, the healing process leads to scar formation, characterized by thicker and stiffer dermis [5], as well as permanent contracture [6]. The molecular components and their effects on cellular signaling pathways during healing have been intensely studied over decades, yet, we still ignore some of the mechanobiological aspects and how the signaling cascades integrate synchronously in space and time to restore mechanical function [7,8,6].

The elusiveness of a solution to perfect tissue regeneration is a consequence of the complex nature of the healing process. Complexity in living materials arises from the multi-scale interaction of an intricate regulatory circuitry. Mechanical forces, microstructural cues and a rich set of chemokine gradients, affect cellular actions which in turn feed back into the signaling network [9] (see Fig. 1). During wound healing, production and diffusion of chemical signals such as platelet derived growth factor (PDGF) and transforming growth factor $\beta$ (TGF-$\beta$) attract macrophages and fibroblasts [10]. Macrophages maintain production of TGF-$\beta$ and release other factors including transforming growth factor $\alpha$ (TGF-$\alpha$), fibroblast growth factors (FGF), and vascular endothelial growth factor (VEGF) [11]. TGF-$\alpha$ is a chemoattractant for keratinocytes, which are in charge of the reepithelialization process [12]. FGF1,2,4 and VEGF regulate endothelial cells during the formation of new vasculature termed angiogenesis [13]. Fibroblasts are the cells in charge of depositing and remodeling the new extra cellular matrix (ECM) [9]. Fibroblasts also produce FGF's involved in reepithelialization and angiogenesis [14]. Beyond deposition of structural proteins, fibroblasts assemble the new ECM into the proper microstructural patterns by acute tissue contraction and fiber realignment that over time leads to permanent remodeling [15,16].

Systems based approaches are a current paradigm in biology that emphasize the need for computational tools in order to elucidate basic mechanisms and dynamics of regulatory pathways [17]. From this perspective, a list of the elements of the system and their relationships is only part of the problem. Intuition built on experimental data alone is not enough to fully understand and ultimately control the healing process at will [18]. In the context of connective tissues, special attention should be given to the role of mechanical cues as key regulators in tissue regeneration [19]. Moreover, understanding healing of living tissues could also inform the design of self-healing materials [20].

From the applied mechanics standpoint, there have also been increasing efforts to adapt classical mechanics concepts and develop new theories that capture the multi-scale hierarchical organization of biological tissues [21], as well as their capabilities to adapt in response to mechanical cues [22]. Significant advances in biomechanics have contributed to the creation of novel biomedical technologies rooted in computational simulations [23]. A preeminent example is the continuum theory of remodeling and volumetric growth [24,25]. As the tools of the applied mechanist and those of the system biologist continue to interact with each other, new and exciting models and theories continue to emerge [26,27]. State of the art examples showcasing continuum mechanics descriptions in biological or biomedical applications include models of growth and morphogenesis in seashells [28], bone growth and remodeling [29], or brain folding [30], to name a few of an expanding list of works in the field. Wound healing modeling has received considerable attention over the past two decades with increasing emphasis on the mechanobiological aspects very recently, see for example [7,31] for comprehensive reviews.

Here we propose a modeling approach to wound healing under the frame of computational systems mechanobiology. To take into account the macroscopic level deformations and spatial distribution of cells and chemokines we start from a continuum model. Making use of the hypothesis that independent kinematic laws can be made at a local microscopic level, we incorporate the well known split of the deformation gradient and allow for the structural parameters to change locally over time [32]. Unlike purely mechanical approaches, we embed a dynamic model of cell-based adaptation in the spirit of systems biology approaches [33]. Consequently, we are able to capture the coupling between cell-based regulatory networks to tissue-level mechanics and chemokine gradients. This manuscript is a natural progression of our previous work on modeling wound healing [34]. In our original investigations we limited our attention to a simple coupling between the mechanics and the biochemical fields; namely, we modeled how the change in collagen content by the cell population affected the mechanical properties of the tissue. Here we refine the constitutive models and include the couplings that we had outlined in our original paper as the logical next steps. Additionally, we introduce constitutive changes in kinematic variables such as the fiber alignment and the permanent deformation by considering an intermediate configuration [24,25]. The implications are not only a sophistication of the constitutive equations with respect to our previous work, but also significant changes in the numerical algorithm.

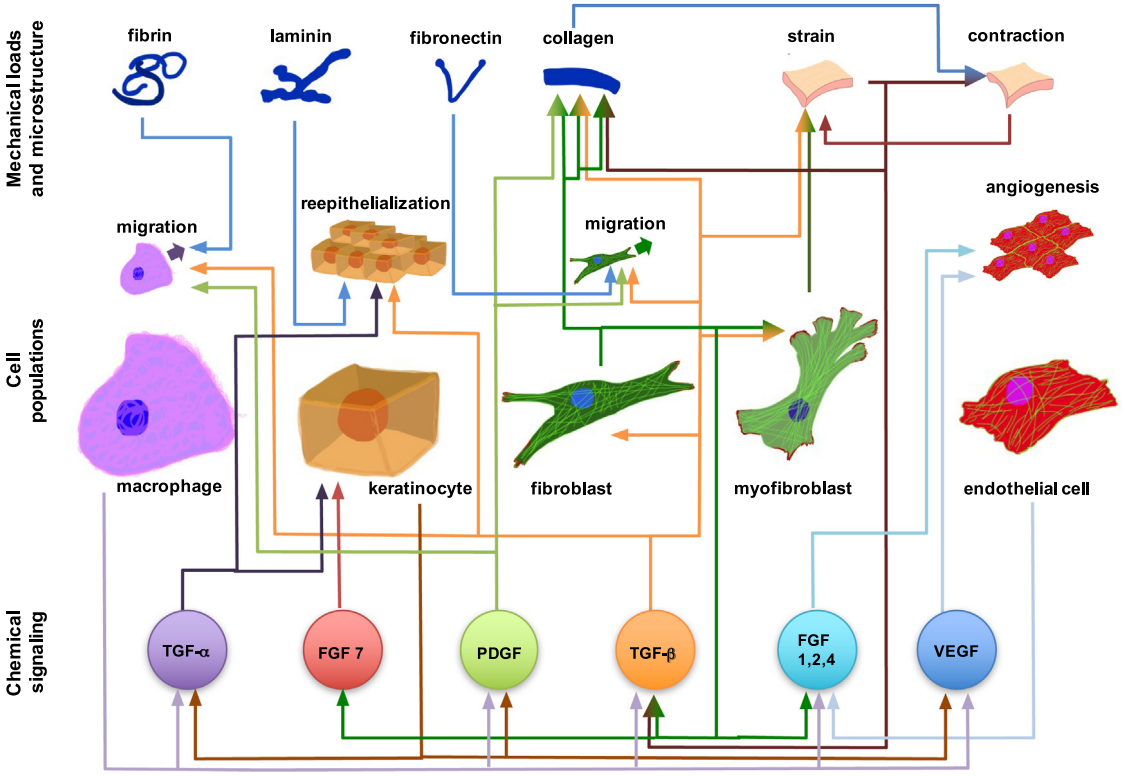


Fig. 1. During wound healing, different cell populations establish a network of chemical signaling pathways and interact with the tissue microstructure in order to coordinate the regenerative process. Macrophages are inflammatory cells that release platelet derived growth factor (PDGF), transforming growth factor *beta* (TGF-$\beta$), and vascular endothelial growth factor (VEGF). Keratinocytes are in charge of re-epithelialization. Endothelial cells migrate and fuse together in a process called angiogenesis, which yields new blood vessels. Fibroblasts are the central cells in terms of mechanical function recovery. Fibroblasts respond to TGF-$\beta$, PDGF and strain by altering their migration, collagen deposition, and proliferation rates. Fibroblasts differentiate into myofibroblasts which can exert forces on their surroundings. The active deformation of their local environment coupled with the deposition of new collagen results in permanent contracture.

We focus on cutaneous wound healing. Skin is a thin membrane consisting of two very different layers. At the outer surface we find the epidermis. The main roles of this layer are to be impermeable and to maintain a continuous turnover of new tissue. The epidermis is a highly cellular construct composed primarily of keratinocytes. These cells are born at the basement membrane and then crawl up to the outer surface before detaching from the body [35]. Below the epidermis we find the dermis, which is the main load bearing layer. The most common cell type found in the dermis is the fibroblast. The dermis is rather acellular compared to the epidermis. The main constituent of the dermis is a collagen network that amounts for 80% of the dry weight of the tissue and that gives skin its mechanical properties [36].

The wound healing process consists of four overlapping stages: hemostasis, inflammation, proliferation, and remodeling [7]. The hemostasis event is the fast creation of a clot to stop blood loss. Platelets from the circulatory system get deposited in the clot, degranulate and release chemotactic signals such as TGF-$\beta$ and PDGF [1]. Then, at the start of the inflammation stage for a period of approximately two days after injury, neutrophils are prevalent in the wound, they produce antimicrobial substances and phagocyte bacteria [37]. Macrophages belong to a secondary phase of prolonged inflammation, their role is to continue the immunological response and to establish a long-lasting chemical source of various cytokines to recruit fibroblasts, endothelial cells, and keratinocytes [37]. TGF-$\alpha$, TGF-$\beta$, FGF, PDGF, and VEGF are the most important cytokines to stimulate mitosis and migration of the native skin cells (see Fig. 1).

The third stage of healing is proliferation. This step shows the most intense regeneration of tissue. During this phase keratinocytes build the new epidermis and fibroblasts assemble the new ECM in the dermis. In the healthy tissue, proliferative keratinocytes are polarized by adhering to the basement membrane, allowing them to establish a

continuous renewal of the epidermis [35]. Upon injury, these cells migrate laterally instead to build a new epidermis over the wounded area [12]. The change in the keratinocyte's phenotype is coupled to the release of growth factors from macrophages and fibroblasts, particularly TGF-$\alpha$ and FGF 7 [14]. Fibroblasts also migrate in respond to the initial inflammatory signals, especially towards PDGF and TGF-$\beta$ [38]. As fibroblasts infiltrate the wound, interaction with the ECM becomes a crucial regulator of the healing process [39]. Fibroblasts show increased collagen deposition in the presence of TGF-$\beta$ [40]. This growth factor also induces differentiation into a contractile phenotype, the myofibroblast, which enables active contraction of the wound [41,42]. The coupling occurs in the opposite direction as well: Mechanotransduction is the mechanism by which cells translate mechanical forces or deformations into chemical signals [43]. Mechanisms of mechanotransduction are shared amongst many cell types of the various connective tissues [44]. In particular for fibroblasts there are three types of mechanical sensors at the cell membrane: integrins, G protein-coupled receptors, and stretch-activated ion channels [19]. Fibroblasts respond to strain by altering their collagen deposition rate and producing TGF-$\beta$ [45,44].

The proliferation stage of wound healing occurs on the order of weeks. By the end of this phase the tissue has regained its functionality, however, its mechanical performance is still poor [46]. Histologically, scar tissue is characterized by thinner collagen bundles with higher degree of alignment [47]. The last phase of the healing process is a very slow operation, on the order of months, termed remodeling [3]. Many cells undergo apoptosis (programmed cell death). The remaining fibroblasts continue to break down the scar and reorganize the ECM, but without the impetus of the proliferative stage. Mature scar tissue is stiffer than healthy skin, yet, intact skin is tougher, even a year after injury [5,47,46].

To model wound healing we first need to organize conceptually how the different pieces fit together in our framework. We classify the key players into three broad categories: cellular populations and their actions; chemical signals; and mechanical cues which include loads and tissue microstructure (see Fig. 1). This classification is accompanied by the specification of the balance equations. For the cells and chemical signals we consider reaction–diffusion systems, for the mechanics problem we consider momentum balance and remodeling. Here we focus on the proliferative and remodeling stages of wound healing in the dermis. The most important cell types for our model are the fibroblast and their contractile phenotype, the myofibroblasts. The inputs for fibroblast activity include strain and TGF-$\beta$. Fibroblasts respond to strain by depositing collagen and producing TGF-$\beta$ [45,44].TGF-$\beta$ contributes to fibroblast migration and collagen deposition [40,44]. TGF-$\beta$ also increases active tissue deformation by myofibroblasts [42]. Over time, as the fibroblasts lay down a new collagen architecture, they effectively cement the deformed state leading to permanent contracture [48]. The relationships between the individual factors define the coupling terms in our model, which we present next.

## 2. Methods

We start at the tissue level and adopt a continuum description for the variables of interest [34]. The cell densities and concentration fields of chemokines obey reaction–diffusion partial differential equations [49]; static mechanical equilibrium is stated as the vanishing of the divergence of the stress tensor. An important development of the present model compared to [34], is to use the multiplicative split of the deformation gradient into permanent and elastic contributions since it allows us to separate the condition of mechanical equilibrium from the local tissue remodeling. Indeed, the split of the deformation gradient assumes the existence of a local microscopic scale at which independent kinematical and constitutive assumptions can be made [50]. We use a strain energy function that is explicitly formulated in terms of microstructural parameters, therefore linking the tissue level mechanics to the microscopic scale remodeling [51], and making it possible to couple the cellular activity as well at a local level. Previously, we have considered a mixture-based approach that accounted only for changes in mass fractions of some constituents [34]. Here, by adding an intermediate configuration, we not only keep track of the mass fractions of the tissue components, we are also able to model more general changes of the microstructure such as fiber realignment and permanent volume change.

At the cell scale, systems of ordinary differential equations are often used to describe the regulatory network controlling the cellular activity [52]. In the framework presented here, we incorporate those types of models to couple locally the cellular activity to the remodeling of its immediate microscopic environment.

Within a finite element implementation, the mechanical equilibrium and reaction–diffusion systems are solved globally in a monolithic manner with a fully implicit scheme similar to [53], while the update of the structural

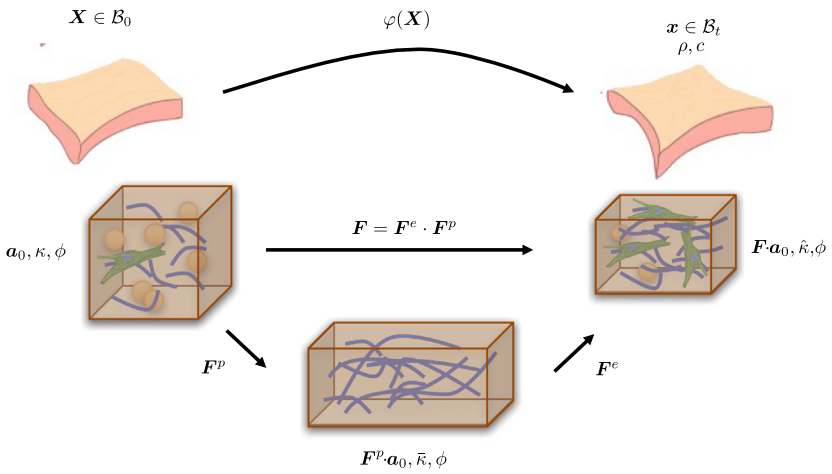


Fig. 2. The kinematic description of mechanobiological systems involves three fields: displacements $\boldsymbol{u}$, cell densities $\rho$, and chemical concentrations $c$. The displacements $\boldsymbol{u}$ express the relationship between material points $\boldsymbol{X} \in \mathcal{B}_0$ and their current position $\boldsymbol{x} = \varphi(\boldsymbol{X}) = \boldsymbol{X} + \boldsymbol{u} \in \mathcal{B}_t$. The gradient $\boldsymbol{F} = \partial \boldsymbol{x}/\partial \boldsymbol{X}$ maps lines, areas and volumes. Following the theory of volumetric growth we split the deformation gradient into permanent and elastic contributions $\boldsymbol{F}^p$ and $\boldsymbol{F}^e$. The microstructure of the tissue in the reference configuration is described by $\boldsymbol{a}_0, \kappa, \phi$ which correspond to fiber direction, dispersion and collagen content respectively. These variables can be expressed in the intermediate and current configurations.

parameters and the permanent deformation tensor are solved at the integration points with an implicit integration scheme. A key development of the current work is the consistent linearization of the finite element residuals. The degrees of freedom at the nodes of the finite elements are the displacements and the concentrations of cells and chemicals. The local degrees of freedom at the integration points are all the variables related to the microstructure. Since the microstructure variables and the nodal degrees of freedom are fully coupled, an additional linear system is solved at the integration points to obtain the consistent linearizations of the finite element residuals.

### 2.1. Kinematics

The reference geometry of the tissue, $\mathcal{B}_0$, is represented by material coordinates $\boldsymbol{X} \subset \mathbb{R}^3$. The current configuration, $\mathcal{B}_t$ at time $t$, is parameterized by the mapping $\boldsymbol{\varphi}$, yielding position vectors $\boldsymbol{x} = \boldsymbol{\varphi}(\boldsymbol{X}) \subset \mathbb{R}^3$ (Fig. 2).

Embedded in the tissue, there are multiple cell populations and chemicals illustrated in Fig. 1. While a full-detail model of wound healing should incorporate all the different cell types and chemokines of this diagram, we lump some of the elements into a few key players to better illustrate the general capabilities of the proposed framework. We restrict our attention to the fibroblast cell density and a single chemical signal concentration, denoted by material fields $\rho(\boldsymbol{X}, t)$ and $c(\boldsymbol{X}, t)$ respectively (Fig. 2). We use the notation $\Xi = \{\boldsymbol{u}, \rho, c\}$ to refer to the global fields.

The cell density field combines the effect of both fibroblasts and myofibroblasts. The chemical field lumps the action of the inflammatory cytokines and mechanotransduction pathways, with emphasis on the mechanisms and effects associated to TGF-$\beta$.

We now zoom in to the microstructure as part of the kinematics definitions. The fields $\lambda_a^p(\boldsymbol{X}, t)$ and $\lambda_s^p(\boldsymbol{X}, t)$ parameterize the local permanent volume change of the tissue driven by the biological variables. In wounds this deformation is often seen as permanent contracture or shrinkage of the tissue [41]. Skin adapts to mechanical cues primarily by permanent deformation in the plane while maintaining the same thickness, therefore $\lambda_a^p(\boldsymbol{X}, t)$ and $\lambda_s^p(\boldsymbol{X}, t)$ directly represent changes in area; however, the end result is a change in volume [54,55]. Skin is an anisotropic material, its mechanical behavior is governed by the presence of collagen fibers with a preferred fiber direction $\boldsymbol{a}_0(\boldsymbol{X}, t)$ and dispersion $\kappa(\boldsymbol{X}, t)$. The fraction of collagen content, $\phi(\boldsymbol{X}, t)$, also changes during the healing process [56–58]. We denote the local variables as $\Theta = \{\phi, \boldsymbol{a}_0, \kappa, \lambda_a^p, \lambda_s^p\}$.

The gradient of the deformation map $\boldsymbol{F} = \partial \boldsymbol{\varphi}/\partial \boldsymbol{X}$ captures the local changes in geometry. We introduce the split of the deformation gradient into permanent and elastic contributions

$$\boldsymbol{F} = \boldsymbol{F}^e \cdot \boldsymbol{F}^p. \tag{1}$$

This split has been widely adopted to describe tissue growth in the biomechanics community [59]. For wound healing, the tensor $\boldsymbol{F}^p$ captures permanent deformation which is not necessarily growth, it also includes contracture [60]. Fig. 1 shows the control loop that reflects how myofibroblasts actively contract the tissue elastically, but then, deposition of new collagen fibers effectively cement the contracted state [41]. The continuous deposition and degradation of collagen coupled with the elastic deformation by myofibroblasts and externally applied forces yields a permanent change in volume represented by $\boldsymbol{F}^p$ (Fig. 2).

Skin is a thin membrane, with outward unit normal $\boldsymbol{N}$ in the reference configuration. The fiber direction $\boldsymbol{a}_0$ is assumed to be in the tangent plane, $\boldsymbol{a}_0 \cdot \boldsymbol{N} = 0$. It is useful to introduce an orthonormal basis $\{\boldsymbol{a}_0, \boldsymbol{s}_0, \boldsymbol{N}\}$ at every point of the reference configuration, such that the permanent deformation tensor can be expressed in this basis as

$$\boldsymbol{F}^p = \lambda_a^p \boldsymbol{a}_0 \otimes \boldsymbol{a}_0 + \lambda_s^p \boldsymbol{s}_0 \otimes \boldsymbol{s}_0 + \boldsymbol{N} \otimes \boldsymbol{N}. \tag{2}$$

The construction of $\boldsymbol{F}^p$ in this manner allows for permanent deformation to occur only in the plane while leaving the normal direction unchanged. Moreover, the vectors $\boldsymbol{a}_0$ and $\boldsymbol{s}_0$ are also eigenvectors of $\boldsymbol{F}^p$ with eigenvalues $\lambda_a^p$ and $\lambda_s^p$ respectively. The area change from the reference to the intermediate configuration is

$$\theta^p = \lambda_a^p \, \lambda_s^p. \tag{3}$$

The definition of $\boldsymbol{F}^p$ in (2) is both kinematic and constitutive. We introduce the structural tensor in the reference configuration

$$\boldsymbol{A}_0 = \kappa \boldsymbol{I}_s + (1 - 2\kappa) \boldsymbol{a}_0 \otimes \boldsymbol{a}_0, \tag{4}$$

which describes a family of fibers with an angular distribution function around the preferred direction $\boldsymbol{a}_0$ [61–63]. The structural tensor originates from integrating a planar, angular fiber distribution over the unit circle [64]. The parameter $\kappa \in [0, 1/2]$ controls the fiber dispersion. When $\kappa = 0$ the structural tensor takes into account the fiber alignment direction only, reducing to $\boldsymbol{a}_0 \otimes \boldsymbol{a}_0$. In the limit of $\kappa = 1/2$, the structural tensor equals the surface identity, denoting a completely isotropic response in the plane. Alternatively, a micro-sphere-based approach can be employed to model the contribution and distribution of fibers in biological tissues [65], and their remodeling [66]. The surface identity

$$\boldsymbol{I}_s = \boldsymbol{I} - \boldsymbol{N} \otimes \boldsymbol{N} = \boldsymbol{a}_0 \otimes \boldsymbol{a}_0 + \boldsymbol{s}_0 \otimes \boldsymbol{s}_0 \tag{5}$$

subtracts the action of the reference unit normal $\boldsymbol{N}$. The elastic component of the deformation gradient is used to define the elastic right and left Cauchy–Green deformation tensors

$$\boldsymbol{C}^e = \boldsymbol{F}^{e\,T} \cdot \boldsymbol{F}^e, \qquad \boldsymbol{b}^e = \boldsymbol{F}^e \cdot \boldsymbol{F}^{e\,T}, \tag{6}$$

respectively. The elastic response of the tissue is characterized in general by the principal invariants and pseudo-invariants of the elastic deformation tensor $\boldsymbol{C}^e$. We recall the definition of the first invariant

$$I_1^e = \mathrm{tr}(\boldsymbol{C}^e) \tag{7}$$

that captures the isotropic response. The fourth pseudo-invariant captures the anisotropic response dominated by the stretch of the fiber direction measured from the intermediate to the deformed configuration. The fifth pseudo-invariant is associated to the stretch of $\boldsymbol{s}_0$,

$$I_4^e = \boldsymbol{a}_0 \cdot \boldsymbol{C}^e \cdot \boldsymbol{a}_0 = (\lambda_a^e)^2, \qquad I_5^e = \boldsymbol{s}_0 \cdot \boldsymbol{C}^e \cdot \boldsymbol{s}_0 = (\lambda_s^e)^2. \tag{8}$$

Note that at the intermediate configuration we have directly substituted $\boldsymbol{a}_0$, $\boldsymbol{s}_0$ defined in the reference configuration because $\boldsymbol{F}^p \cdot \boldsymbol{a}_0 = \boldsymbol{a}_0$, $\boldsymbol{F}^p \cdot \boldsymbol{s}_0 = \boldsymbol{s}_0$: The tensor $\boldsymbol{F}^p$ preserves the direction of anisotropy. We also introduce

$$\boldsymbol{C}_s^e = \boldsymbol{C}^e - \lambda_N^2 \boldsymbol{N} \otimes \boldsymbol{N}, \tag{9}$$

the deformation restricted to the tangent plane. This decomposition is valid in the absence of transverse shear. A definition of $\boldsymbol{C}_s^e$ when transverse shear is allowed is also possible, however, it has been shown that thin biological membranes such as skin can be modeled omitting transverse shear deformations [67], consequently we employ this kinematical assumption in the rest of this work. With respect to the biochemical fields, the choice of a three-dimensional (3D) representation or one parameterized by a two-dimensional (2D) surface is application dependent.

In our previous work [34] we showed a 3D model, yet, we mainly focused on the in-plane behavior. Clinically, 2D metrics of wound healing such as wound contraction or epithelialization are prevalent and they show little variation through the thickness [68]. Nevertheless, A 3D model could be beneficial in certain cases, for example in the modeling of healing with the use of vacuum assisted closure devices which explicitly consider the role of deformations through the thickness due to the application of pressure in the direction normal to the skin plane [69].

The surface portion of the deformation is used to define the area change and the first invariant restricted to the tangent plane

$$\theta^e = \sqrt{\det(\boldsymbol{C}_s^e + \boldsymbol{N}\otimes\boldsymbol{N})}, \qquad I_{1,s} = \mathrm{tr}(\boldsymbol{C}_s^e). \tag{10}$$

Moreover, imposing incompressibility, the stretch of the normal comes only from the elastic component of the deformation gradient

$$\lambda_N = \|\boldsymbol{F}\cdot\boldsymbol{N}\| = \|\boldsymbol{F}^e\cdot\boldsymbol{N}\| = (\theta^e)^{-1}. \tag{11}$$

The elastic deformation can also be characterized in terms of the principal stretches of $\boldsymbol{C}_s^e$. Let $\boldsymbol{e}_\alpha$, $\alpha = \{0, 1\}$, be such that

$$\boldsymbol{C}_s^e\cdot\boldsymbol{e}_\alpha = \lambda_\alpha^2\boldsymbol{e}_\alpha \tag{12}$$

and $\lambda_1 \geq \lambda_0$. Then another useful representation of the elastic deformation is

$$\boldsymbol{C}^e = \lambda_\alpha^2\,\boldsymbol{e}_\alpha\otimes\boldsymbol{e}_\alpha + \lambda_N^2\boldsymbol{N}\otimes\boldsymbol{N}, \tag{13}$$

where the summation convention was used. The elastic deformation will not preserve the direction of anisotropy in general. Fibers in the direction $\boldsymbol{a}_0$ get mapped to $\boldsymbol{a} = \boldsymbol{F}\boldsymbol{a}_0$ in the current configuration. Furthermore, the push-forward of the structural tensor is

$$\boldsymbol{A} = \boldsymbol{F}\cdot\boldsymbol{A}_0\cdot\boldsymbol{F}^T = \kappa\boldsymbol{b} + (1-2\kappa)\boldsymbol{a}\otimes\boldsymbol{a}, \tag{14}$$

with $\boldsymbol{b} = \boldsymbol{F}\cdot\boldsymbol{F}^T$. However, the tensor $\boldsymbol{A}$ is no longer a valid structural tensor to represent the new distribution of the fibers in the current configuration because its trace is not one [61]. The actual structural tensor corresponding to the deformed state is obtained by normalizing the push-forward of $\boldsymbol{A}_0$ [70]

$$\hat{\boldsymbol{A}} = \frac{\boldsymbol{A}}{\mathrm{tr}(\boldsymbol{A})} = \hat{\kappa}\boldsymbol{i}_s + (1-2\hat{\kappa})\hat{\boldsymbol{a}}\otimes\hat{\boldsymbol{a}}, \tag{15}$$

where $\hat{\kappa}$ is the fiber dispersion in the current configuration, $\hat{\boldsymbol{a}} = \boldsymbol{a}/\|\boldsymbol{a}\|$ is the normalized fiber direction, and $\boldsymbol{i}_s$ is the surface identity, all defined in the current configuration. Recalling the orthonormal basis in the reference configuration $\{\boldsymbol{a}_0, \boldsymbol{s}_0, \boldsymbol{N}\}$, the deformation gradient can be expressed as

$$\boldsymbol{F} = \boldsymbol{a}\otimes\boldsymbol{a}_0 + \boldsymbol{s}\otimes\boldsymbol{s}_0 + \lambda_N\boldsymbol{n}\otimes\boldsymbol{N}, \tag{16}$$

with $\boldsymbol{s} = \boldsymbol{F}\cdot\boldsymbol{s}_0$, $\lambda_N\boldsymbol{n} = \boldsymbol{F}\cdot\boldsymbol{N}$. The left Cauchy–Green deformation tensor becomes

$$\boldsymbol{b} = \boldsymbol{a}\otimes\boldsymbol{a} + \boldsymbol{s}\otimes\boldsymbol{s} + \lambda_N^2\boldsymbol{n}\otimes\boldsymbol{N}, \tag{17}$$

and the push forward of the structural tensor can be written in terms of the deformed covariant vectors $\{\boldsymbol{a}, \boldsymbol{s}\}$

$$\boldsymbol{A} = \kappa\boldsymbol{s}\otimes\boldsymbol{s} + (1-\kappa)\boldsymbol{a}\otimes\boldsymbol{a}. \tag{18}$$

Let $\boldsymbol{r}$ be a unit vector orthogonal to both $\boldsymbol{a}$ and $\boldsymbol{n}$. Then the fiber dispersion in the current configuration can be explicitly computed

$$\hat{\kappa} = \frac{\kappa(\boldsymbol{r}\cdot\boldsymbol{s})^2}{\mathrm{tr}(\boldsymbol{A})}. \tag{19}$$

A similar derivation shows that the fiber dispersion changes also at the intermediate configuration

$$\bar{\kappa} = \frac{\kappa(\lambda_s^p)^2}{\kappa(\lambda_s^p)^2 + (1-\kappa)(\lambda_a^p)^2}. \tag{20}$$

### 2.2. Balance laws

#### 2.2.1. Mechanical equilibrium

To satisfy mechanical equilibrium, we require the vanishing of the stress in the absence of body forces,

$$\nabla_x \cdot \boldsymbol{\sigma} = \mathbf{0}. \tag{21}$$

In addition to the passive material response, myofibroblasts contribute actively to deform the ECM [6]. We assume an additive split of the stress into a pressure term as well as passive, and active contributions,

$$\boldsymbol{\sigma} = \boldsymbol{\sigma}^{\text{pas}} + \boldsymbol{\sigma}^{\text{act}} + p\boldsymbol{I}. \tag{22}$$

Considering the skin to behave as an incompressible hyper elastic material, the passive material response is fully determined by a scalar function, the strain energy $\psi$ per unit reference volume. The Cauchy stress comes from differentiating with respect to the elastic right Cauchy–Green deformation tensor to get the second Piola–Kirchhoff stress $\boldsymbol{S}^{e,\text{pas}}$, and performing the appropriate Piola transformation

$$\boldsymbol{\sigma}^{\text{pas}} = \frac{2}{J^e}\boldsymbol{F}^e \cdot \frac{\partial \psi}{\partial \boldsymbol{C}^e} \cdot \boldsymbol{F}^{eT} = \frac{1}{J^e}\boldsymbol{F}^e \cdot \boldsymbol{S}^{e,\text{pas}} \cdot \boldsymbol{F}^{eT}. \tag{23}$$

The active stress is a function of the cell density field. Fibroblasts and especially myofibroblasts pull along the collagen fibers, and their contraction can be influenced by the TGF-$\beta$ concentration [41]. In our case,

$$\boldsymbol{\sigma}^{\text{act}} = \phi\, t(\rho, c)\, \hat{\boldsymbol{A}}, \tag{24}$$

such that a stress of magnitude $t(\rho, c)$, a function of the cell density and the chemical concentration, gets weighted by the collagen fraction $\phi$, and acts on the normalized structural tensor at the current configuration.

We have presented the stress tensors in the current configuration. One of the reasons for this choice is that the active stress exerted by the cells is naturally expressed in terms of the kinematics of the deformed state. Alternatively, the formulation of the mechanical equilibrium problem in the reference configuration is

$$\nabla_X \cdot \boldsymbol{P} = \mathbf{0}, \tag{25}$$

where the operator $\nabla_X \cdot (\bullet)$ denotes the divergence in the reference configuration; and the tensor $\boldsymbol{P} = J\boldsymbol{\sigma} \cdot \boldsymbol{F}^{-T}$ is the first Piola–Kirchhoff stress tensor. In particular, the pull back of the active part of the stress is

$$\boldsymbol{S}^{\text{act}} = \frac{\theta^p \phi\, t(\rho, c)}{\text{tr}(\boldsymbol{A})}\boldsymbol{A}_0, \tag{26}$$

whereas the pull back of the passive part has been defined already in Eq. (23).

#### 2.2.2. Mass balance of the biological fields

The cell population and the chemical concentration fields obey standard reaction–diffusion systems,

$$\begin{aligned} \dot{\rho} + \nabla_x \cdot \boldsymbol{q}_\rho(\rho, c) &= s_\rho(\rho, c, \boldsymbol{F}, \boldsymbol{F}^p), \\ \dot{c} + \nabla_x \cdot \boldsymbol{q}_c(c) &= s_c(\rho, c, \boldsymbol{F}, \boldsymbol{F}^p), \end{aligned} \tag{27}$$

where $\dot{(\bullet)}$ denotes the material time derivative. The flux and source term of the cell density are coupled to the chemical concentration. More importantly, the chemical and cell source terms consider a coupling to the mechanics through $\boldsymbol{F}, \boldsymbol{F}^p$. The dependency of $s_\rho$ on the state of deformation encodes the direct mechanotransduction pathways of fibroblasts [44]. The dependency of $s_c$ on the deformation is motivated by the fact that TGF-$\beta$ is a secondary messenger in the mechanosensing response (Fig. 1). The material description of the balance law is

$$\begin{aligned} J\dot{\rho} + \nabla_X \cdot \boldsymbol{Q}_\rho(\rho, c) &= J\, s_\rho(\rho, c, \boldsymbol{F}, \boldsymbol{F}^p), \\ J\dot{c} + \nabla_X \cdot \boldsymbol{Q}_c(c) &= J\, s_c(\rho, c, \boldsymbol{F}, \boldsymbol{F}^p), \end{aligned} \tag{28}$$

with the material fluxes defined as $\boldsymbol{Q}_\rho = J\boldsymbol{F}^{-1}\boldsymbol{q}_\rho$, $\boldsymbol{Q}_c = J\boldsymbol{F}^{-1}\boldsymbol{q}_c$. The source terms in the reference are $S_\rho = J\, s_\rho$, $S_c = J\, s_c$, and the reference fields for cells and chemokines are $\rho_0 = J\rho$, $c_0 = Jc$.

*2.2.3. Local remodeling*

Tissue remodeling occurs locally, so that the evolution in time of the structural parameters obey a system of ordinary differential equations at every point. The collagen deposition is affected by the cell population in response to the chemical signaling and the elastic deformation

$$\dot{\phi} = f_\phi(\rho, c, \boldsymbol{F}, \boldsymbol{F}^p, \phi). \tag{29}$$

The rate of collagen deposition is a crucial component of the remaining remodeling rules. The fibers get reoriented with angular velocity $\omega$,

$$\dot{\boldsymbol{a}}_0 = \boldsymbol{R}(\omega t) \cdot \boldsymbol{a}_0, \tag{30}$$

where $\boldsymbol{R}(\omega t)$ is a rotation around the normal $\boldsymbol{N}$ [71]. The angular velocity is a function of the rate of collagen deposition and the elastic deformation. Similar dependencies can be stated for the other remodeling variables

$$\begin{aligned} \dot{\kappa} &= f_\kappa(\boldsymbol{F}, \boldsymbol{F}^p, \dot{\phi}, \kappa), \\ \dot{\lambda}_a^p &= f_{\lambda_a}(\boldsymbol{F}, \boldsymbol{F}^p, \dot{\phi}, \lambda_a^p), \\ \dot{\lambda}_s^p &= f_{\lambda_s}(\boldsymbol{F}, \boldsymbol{F}^p, \dot{\phi}, \lambda_s^p). \end{aligned} \tag{31}$$

We remark that the structural variables, with the exception of $\phi$, do not depend explicitly on the cell population density or the chemical signal, rather, the critical dependency is the production of new collagen. Moreover, here we state simply that the local variables change according to a system of ordinary differential equations, but we still need to specify the specific form of these as we will see in the next section.

*2.3. Constitutive equations*

*2.3.1. Stress*

The strain energy function describing the passive material behavior of the skin consists of the isotropic ECM response and the fiber contribution weighted by the collagen fraction

$$\begin{aligned} \psi &= \psi^m + \phi\, \psi^f, \\ \psi^m &= k_0[I_1^e - 3], \\ \psi^f &= \frac{k_f}{2k_2}[\exp(k_2\,[\,\kappa\, I_{1,s}^e + [1-2\kappa]\, I_4^e - 1]^2) - 1]. \end{aligned} \tag{32}$$

The passive second Piola–Kirchhoff elastic stress tensor

$$S^{e,\text{pas}} = 2\frac{\partial \psi}{\partial \boldsymbol{C}^e} = k_0 \boldsymbol{I} + \phi\, (\psi_1^f \boldsymbol{I}_s + \psi_4^f \hat{\boldsymbol{a}}_0^e \otimes \hat{\boldsymbol{e}}_0^e) \tag{33}$$

requires the derivatives $\psi_1^f = \partial\psi/\partial I_{1,s}$ and $\psi_4^f = \partial\psi/\partial I_4$ which explicitly read

$$\begin{aligned} \psi_1^f &= 2\,k_2\kappa[\,\kappa\, I_{1,s} + [\,1-2\kappa\,]I_4 - 1\,]\psi^f, \\ \psi_4 &= 2\,k_2[1-2\kappa][\,\kappa\, I_{1,s} + [\,1-2\kappa\,]I_4 - 1\,]\psi^f. \end{aligned} \tag{34}$$

The active stress is exerted by the cell population. The magnitude of the stress is determined by the function

$$t(\rho, c) = \left(\tau_f + \frac{\tau_{m,c}\, c}{K_{\tau,c} + c}\right)\rho, \tag{35}$$

which takes into account that fibroblast can exert tractions with magnitude $\tau_f$ while the myofibroblast contraction is enhanced by the TGF-$\beta$ concentration which in this case is considered an essential part of the chemical field $c$. Due to the presence of the chemical signaling, the cell population can exert tractions on the order of $\tau_{m,c}\, c$. The parameter $K_{\tau,c}$ controls the saturation response of the cells with respect to the chemical.

To fully determine the state of stress, the pressure Lagrange multiplier can be solved for explicitly imposing the plane stress condition

$$p = -k_0 \lambda_N^2. \tag{36}$$

*2.3.2. Flux and source terms for the biological fields*

The balance law for the cell density field requires a constitutive definition of the flux and source terms. Cell migration can be considered a combination of random motion and directed migration in the direction of the chemical gradient [72]

$$\boldsymbol{Q}_\rho = -D^{\rho\rho}\,\boldsymbol{C}^{-1}\nabla_X\,\rho - D^{\rho c}\,\rho\boldsymbol{C}^{-1}\,\nabla_X\,c. \tag{37}$$

On the other hand, the source term

$$s_\rho = \left(p_{\rho,n} + \frac{p_{\rho,c}c}{K_{\rho,c}+c} + p_{\rho,e}\hat{H}(\theta^e - \vartheta^e)\right)\left(1 - \frac{\rho}{K_{\rho\rho}}\right)\rho - d_\rho\,\rho, \tag{38}$$

reflects a physiological mitotic rate $p_{\rho,n}$ that can be increased by the presence of the chemical concentration or elastic deformation up to $p_{\rho,c}$ and $p_{\rho,e}$. In biological systems modeling, Michaelis–Menten kinetics are employed to describe interactions between proteins in signaling pathways [73]. For example, in this case, the chemical signal $c$ affects the pathway in the cell related to cell division [74]. The logistic term accounting for a cell carrying capacity of the tissue is also a common choice in the modeling of biological systems [75]. The logistic function

$$\hat{H}(\theta^e - \vartheta^e) = \frac{1}{1+\exp(-\gamma_\theta(\theta^e - \vartheta^e))}, \tag{39}$$

with parameters $\gamma_\theta$, $\vartheta^e$, controls how the mechanotransduction pathway gets activated. A mechanosensing model has been previously proposed incorporating volumetric strains as an input and assuming that the mechanosensing variable is the active pressure transmitted to the ECM by a single cell [75]. On the other hand, stretch activated ion channels have been described with logistic functions where the exponential term depends on sarcomere stretch and a sensitivity parameter [76]. Activation of ion channels is one mechanism of mechanotransduction in fibroblasts [44]. Mechanotransduction could also be modeled by considering adhesion binding dynamics between the cell and the substrate[77]. We choose a logistic function since it offers a smooth switching behavior and a saturation response. Experimental observations suggest that different strain magnitudes and time scales could be related to different mechanotransduction mechanisms, for example fibroblasts respond differently to strains on the order of 20% compared to 40% [78]. In our case, moderate strains are expected, leading to increased fibroblast proliferation [45]. However, while the connection between strain and fibroblast response is clear, further analysis is needed to justify the choice of Eq. (39) or an alternative.

For the chemokine, flux is due to diffusion only

$$\boldsymbol{Q}_c = -D^{cc}\boldsymbol{C}^{-1}\,\nabla_X\,c. \tag{40}$$

The source term also captures the mechanosensing capabilities of fibroblasts. The chemokine $c$ is assumed a secondary messenger in the mechanosensing response, and is thus directly affected by the elastic deformation

$$s_c = \left(p_{c,\rho}c + p_{c,e}\hat{H}(\theta^e - \vartheta^e)\right)\left(\frac{\rho}{K_{c,c}+c}\right) - d_c\,c. \tag{41}$$

There is also a feed forward loop parameterized by $p_{c,\rho}$ that depends on the cell density and the chemical concentration as illustrated in Fig. 1. Once more we have modeled the interactions between the components in the signaling network using Michaelis–Menten kinetics following examples in the literature [73–75].

*2.3.3. Remodeling laws*

At the local level, the fractional amount of collagen evolves in a form analogous to the production of chemical by the cells. The deposition of new collagen is affected by the chemokine and the mechanosensing mechanism [79],

$$\dot{\phi}_+ = \left(p_{\phi,n} + \frac{p_{\phi,c}\,c}{K_{\phi,c}+c} + p_{\phi,e}\hat{H}(\theta^e - \vartheta^e)\right)\left(\frac{\rho}{K_{\phi,\rho}+\phi}\right), \tag{42}$$

so that the net change in collagen fraction, incorporating a decay term, is

$$\dot{\phi} = f_\phi = \dot{\phi}_+ - (d_\phi + c\,\rho d_{\phi,c})\,\phi. \tag{43}$$

It has been observed that cells can reorient the collagen fibers over time [25]. Aligning $\boldsymbol{a}_0$ with the principal stretch direction is one hypothesis for remodeling based on the fact that the free energy reaches a critical point in such scenario [71]. This hypothesis is supported by the experimental evidence showing that fibers under tension are less likely to be degraded compared to unstressed fibers [48]. We introduce an angular rate of reorientation

$$\omega = \frac{2\pi\dot{\phi}_+}{\tau_\omega}\sin(\alpha)\lambda_1^2, \tag{44}$$

where $\sin(\alpha) = \boldsymbol{a}_0 \times \boldsymbol{e}_1$, namely, $\alpha$ is the angle between the anisotropy vector and the first principal stretch direction. The parameter $\tau_\omega$ plays the role of a time constant. The reorientation process is directly affected by the rate of collagen deposition $\dot{\phi}_+$. This dependence is motivated by the work presented in [48,80], where rather than considering an immutable fiber architecture that is reoriented over time, fibers are added primarily along the principal stretch direction, and those in the perpendicular direction are more likely to be degraded over time. The angular velocity and the normal to the tangent plane define a rotation tensor. Using Rodrigues formula

$$\boldsymbol{R}(\omega t) = \cos(\omega t)\boldsymbol{I} + (1-\cos(\omega t))\boldsymbol{N}\otimes\boldsymbol{N} + \sin(\omega t)\boldsymbol{N}^\star. \tag{45}$$

The tensor $\boldsymbol{N}^\star$ is the skew-symmetric second order tensor defined by $\boldsymbol{N}^\star\cdot\boldsymbol{v} = \boldsymbol{N}\times\boldsymbol{v}$ for arbitrary $\boldsymbol{v}$. The structural parameter $\kappa$ also evolves in time [70]. We suggest a simple law which hypothesizes that the fiber dispersion can be driven by the ratio between the in-plane principal stretches,

$$\dot{\kappa} = \left(\frac{\phi_+}{\tau_\kappa}\right)\left(\frac{1}{2}\left(\frac{\lambda_0}{\lambda_1}\right)^{\gamma_\kappa} - \kappa\right). \tag{46}$$

As the ratio of the principal stretches reaches an isotropic deformation $\lambda_0/\lambda_1 \to 1$, $\kappa \to 1/2$; and as the ratio becomes smaller, $\lambda_0/\lambda_1 \to 0$, then $\kappa \to 0$ exponentially depending on $\gamma_\kappa$. This is similar to the approach described in [51,81] where the driving force is also the ratio of the principal stretches. The rate of change of the dispersion parameter is weighted by the deposition of new collagen fibers and $\tau_\kappa$ is a time constant.

It remains to specify the permanent tissue contracture parameterized by $\lambda_a^p$ and $\lambda_s^p$. Once more, the key coupling to the global biological and mechanical fields is through the collagen deposition rate $\dot{\phi}_+$,

$$\dot{\lambda}_a^p = \frac{\dot{\phi}_+}{\tau_a}(\lambda_a^e - 1), \qquad \dot{\lambda}_s^p = \frac{\dot{\phi}_+}{\tau_s}(\lambda_s^e - 1). \tag{47}$$

### 2.4. Discrete residuals

We solve the set of equations outlined in the preceding sections using the finite element method. To derive the discrete version of the residuals we first recast the global problem in its weak form in the reference configuration. We remark that up to this point we had kept both the material and spatial descriptions in an effort to achieve a thorough definition of the problem. However we now present only the numerical algorithm based on the material description. We recall the notation $\Xi(\boldsymbol{X},t) \equiv \{\boldsymbol{u}(\boldsymbol{X},t), \rho(\boldsymbol{X},t), c(\boldsymbol{X},t)\} \in \mathcal{V} = \mathcal{V}^u \times \mathcal{V}^\rho \times \mathcal{V}^c$. We look for $\Xi(\boldsymbol{X},t)$ such that

$$\begin{aligned}
&\int_{\mathcal{B}_0} \frac{1}{2}\boldsymbol{S} :\ D(\boldsymbol{C})[\delta\boldsymbol{u}]\mathrm{dV} - \int_{\partial\mathcal{B}_0^t} \boldsymbol{t}\cdot\boldsymbol{u}\mathrm{dA} = 0,\\
&\int_{\mathcal{B}_0} \left(J\left(\dot{\rho} - s_\rho\right)\delta\rho - \nabla_X\,\delta\rho\cdot\boldsymbol{Q}_\rho\right)\mathrm{dV} + \int_{\partial\mathcal{B}_0^\rho} Q_{\rho,n}\delta\rho\mathrm{dA} = 0,\\
&\int_{\mathcal{B}_0} \left(J\left(\dot{c} - s_c\right)\delta c - \nabla_X\,\delta c\cdot\boldsymbol{Q}_c\right)\mathrm{dV} + \int_{\partial\mathcal{B}_0^c} Q_{c,n}\delta c\mathrm{dA} = 0,
\end{aligned} \tag{48}$$

for all $\delta\Xi = \{\delta\boldsymbol{u}, \delta\rho, \delta c\} \in \mathcal{W}$. The spaces $\mathcal{V}^u$, $\mathcal{V}^\rho$, $\mathcal{V}^c$, are the standard $H^1$ spaces of functions with square-integrable derivatives satisfying Dirichlet boundary conditions. The Neumann boundary conditions enter the weak form through the boundary integrals in (48). The spaces for the test functions, $\mathcal{W} = \mathcal{W}^u \times \mathcal{W}^\rho \times \mathcal{W}^c$ satisfy homogeneous Dirichlet boundary conditions. Initial conditions $\Xi_0(\boldsymbol{X}) \equiv \Xi(\boldsymbol{X},0)$ are also specified.

We recall the use of a similar notation for the fields describing the local microstructure $\Theta(\boldsymbol{X},t) \equiv \{\phi_f(\boldsymbol{X},t), \boldsymbol{a}_0(\boldsymbol{X},t), \kappa(\boldsymbol{X},t), \lambda_a^p(\boldsymbol{X},t), \lambda_s^p(\boldsymbol{X},t)\}$. The variables $\Theta(\boldsymbol{X},t)$ are treated as $C^{-1}$ fields. The equations describing the

temporal evolution of the structural variables are satisfied locally everywhere in the domain, thus the strong form of the equations is used directly.

We first discretize the time domain by subdividing it into steps of magnitude $\Delta t$. At time $t$ the mechanical and biological fields are denoted via a subscript $\Xi_t(\boldsymbol{X})$. The value of those variables at time $t+\Delta t$ is denoted $\Xi(\boldsymbol{X})$, without a subscript. Using a backward-Euler scheme for the time derivatives and ignoring for now the contribution from the boundary terms, the semi-discrete version of the weak form in the reference configuration of the problem reads

$$\begin{aligned}
&\int_{\mathcal{B}_0} \frac{1}{2}\boldsymbol{S}:\ D(\boldsymbol{C})[\delta\boldsymbol{u}]\mathrm{dV} = 0,\\
&\int_{\mathcal{B}_0} \left(\left(\frac{\rho_0-\rho_{0t}}{\Delta t} - S_\rho\right)\delta\rho - \nabla_X\delta\rho\cdot\boldsymbol{Q}_\rho\right)\mathrm{dV} = 0,\\
&\int_{\mathcal{B}_0} \left(\left(\frac{c_0-c_{0t}}{\Delta t} - S_c\right)\delta c - \nabla_X\delta c\cdot\boldsymbol{Q}_c\right)\mathrm{dV} = 0.
\end{aligned} \tag{49}$$

We use a similar notation for the structural variables. At time $t$ the microstructure of the tissue is determined by $\Theta_t(\boldsymbol{X})$, while $\Theta(\boldsymbol{X})$ refers to the time $t+\Delta t$. We use also a backward-Euler scheme for the time derivatives of the local quantities.

We discretize the spatial domain by means of finite elements. The theory presented in the preceding sections is valid for thin shells. However, for illustrative and clarity purposes here we will restrict the numerical implementation to planar geometries. We use linear quadrilateral elements. Associated to a node $\{a\}$ and an element $\{e\}$ of the finite element mesh there is a local basis function $N_a^e$. The global fields $\Xi$ are linearly interpolated inside each element by $\Xi^e = N_a^e\,\Xi_a^e$, where $\Xi_a^e$ are the values at the nodes. Solution of the weak form of the problem requires integration over each finite element. For linear quadrilateral elements we use the standard $2\times 2$ Gauss quadrature rule. The fields related to the microstructure of the tissue are discretized by their values $\Theta_b^e$ at the integration point $\{b\}$ of element $\{e\}$.

The discrete residuals for the global variables $\Xi_A$ at the node $\{A\}$ are

$$\begin{aligned}
\mathbf{R}_A^u &= \mathop{\mathbf{A}}_{e=1}^{n_{\mathrm{el}}}\int_{\mathcal{B}_0^e}\nabla_X N_a^e\cdot(\boldsymbol{F}\cdot\boldsymbol{S})\mathrm{dV} = 0,\\
\mathrm{R}_A^\rho &= \mathop{\mathbf{A}}_{e=1}^{n_{\mathrm{el}}}\int_{\mathcal{B}_0^e}\left(\left(\frac{\rho_0-\rho_{0t}}{\Delta t} - S_\rho\right)N_a^e - \nabla_X N_a^e\cdot\boldsymbol{Q}_\rho\right)\mathrm{dV} = 0,\\
\mathrm{R}_A^c &= \mathop{\mathbf{A}}_{e=1}^{n_{\mathrm{el}}}\int_{\mathcal{B}_0^e}\left(\left(\frac{c_0-c_{0t}}{\Delta t} - S_c\right)N_a^e - \nabla_X N_a^e\cdot\boldsymbol{Q}_c\right)\mathrm{dV} = 0.
\end{aligned} \tag{50}$$

The nodes $\{a\}$ and $\{A\}$ are related by a mapping from the element to the global degrees of freedom. The operator $\mathbf{A}$ is the standard finite element assembly process. The discrete residuals of the local structural variables at the corresponding integration point are

$$\begin{aligned}
\mathrm{R}^\phi &= \frac{-\phi+\phi_t}{\Delta t} + \left(p_{\phi,n} + \frac{p_{\phi,c}\,c}{K_{\phi,c}+c} + p_{\phi,e}\hat{H}(\theta^e-\vartheta^e)\right)\left(\frac{\rho}{K_{\phi,\rho}+\phi}\right) - (d_\phi + c\,\rho d_{\phi,c})\,\phi = 0,\\
\mathbf{R}^a &= \boldsymbol{a}_0 - \boldsymbol{R}(\omega\Delta t)\boldsymbol{a}_{0,t} = 0,\\
\mathrm{R}^\kappa &= \left(\frac{\phi_+}{\tau_\kappa}\right)\left(\frac{1}{2}\left(\frac{\lambda_0}{\lambda_1}\right)^{\gamma_\kappa} - \kappa\right) = 0,\\
\mathrm{R}^{\lambda_a} &= \frac{-\lambda_a^p + \lambda_{a,t}^p}{\Delta t} + \frac{\dot{\phi}_+}{\tau_a}(\lambda_a^e - 1) = 0,\\
\mathrm{R}^{\lambda_s} &= \frac{-\lambda_s^p + \lambda_{s,t}^p}{\Delta t} + \frac{\dot{\phi}_+}{\tau_s}(\lambda_s^e - 1) = 0.
\end{aligned} \tag{51}$$

### 2.5. Consistent linearization

Both the global and local residuals are non-linear functions and we employ Newton–Raphson iterative algorithms to solve for their roots. The new guess at each iteration relies on a consistent linearization of the residuals. First

we focus on the local problem. Let $\mathbf{R}^{\Theta}$ be the vector containing the residuals (51), and $\mathrm{d}\Theta$ a vector containing the increments $\{\mathrm{d}\phi_f, \mathrm{d}\boldsymbol{a}_0, \mathrm{d}\kappa, \mathrm{d}\lambda_a^p, \mathrm{d}\lambda_s^p\}$. A Taylor expansion of the local residuals yields

$$\mathbf{R}^{\Theta} + \mathbf{K}^{\Theta\Theta} \cdot \mathrm{d}\Theta = 0, \tag{52}$$

where the components of the tangent matrix $\mathbf{K}^{\Theta\Theta}$ are nothing more than the partial derivatives $\partial \mathbf{R}^{\Theta}/\partial\Theta$ of the vector of residuals with respect to the vector of local variables. A Taylor expansion of the global residuals (50) yields

$$\begin{aligned}
\mathbf{R}_A^u + \sum_{L=1}^{n_u} \mathbf{K}_{AL}^{uu} \Delta \boldsymbol{u}_L + \sum_{L=1}^{n_c} \mathbf{K}_{AL}^{uc} \Delta c_L, + \sum_{L=1}^{n_\rho} \mathbf{K}_{AL}^{u\rho} \Delta \rho_L &= 0, \\
\mathrm{R}_A^\rho + \sum_{L=1}^{n_u} \mathbf{K}_{AL}^{\rho u} \Delta \boldsymbol{u}_L + \sum_{L=1}^{n_c} \mathbf{K}_{AL}^{\rho c} \Delta c_L, + \sum_{L=1}^{n_\rho} \mathbf{K}_{AL}^{\rho\rho} \Delta \rho_L &= 0, \\
\mathrm{R}_A^c + \sum_{L=1}^{n_u} \mathbf{K}_{AL}^{cu} \Delta \boldsymbol{u}_L + \sum_{L=1}^{n_c} \mathbf{K}_{AL}^{cc} \Delta c_L, + \sum_{L=1}^{n_\rho} \mathbf{K}_{AL}^{c\rho} \Delta \rho_L &= 0.
\end{aligned} \tag{53}$$

The global tangent matrices for the residual associated to the problem of mechanical equilibrium can be expanded

$$\begin{aligned}
\mathbf{K}_{AL}^{uu} &= \mathop{\mathbf{A}}_{e=1}^{n_{\mathrm{el}}} \int_{\mathcal{B}_0^e} \left( \left( \nabla_X N_a^e \cdot \nabla_X N_l^e \right) \boldsymbol{S} + 2\, \nabla_X N_a^e \cdot \boldsymbol{F} \cdot \mathbb{C}^{uu} \cdot \boldsymbol{F}^T \cdot \nabla_X N_l^e \right) \mathrm{dV}, \\
\mathbf{K}_{AL}^{u\rho} &= \mathop{\mathbf{A}}_{e=1}^{n_{\mathrm{el}}} \int_{\mathcal{B}_0^e} (\nabla_X N_a^e \cdot \boldsymbol{F} \cdot \mathbb{C}^{u\rho}) N_l^e \mathrm{dV}, \\
\mathbf{K}_{AL}^{uc} &= \mathop{\mathbf{A}}_{e=1}^{n_{\mathrm{el}}} \int_{\mathcal{B}_0^e} (\nabla_X N_a^e \cdot \boldsymbol{F} \cdot \mathbb{C}^{uc}) N_l^e \mathrm{dV},
\end{aligned} \tag{54}$$

where the nodes $\{l\}$ and $\{L\}$ are related by the mapping from the element to the global degrees of freedom. We have introduced the total algorithmic derivatives $\mathbb{C}^{uu} = \mathrm{d}\boldsymbol{S}/\mathrm{d}\boldsymbol{C}$, $\mathbb{C}^{u\rho} = \mathrm{d}\boldsymbol{S}/\mathrm{d}\rho$, $\mathbb{C}^{uc} = \mathrm{d}\boldsymbol{S}/\mathrm{d}c$. In contrast to the local system of equations, these derivatives are not just the partial derivatives with respect to the global fields. This would be generally the case for a typical elasticity problem. Here, however, it is crucial to note the that the structural variables also change due to increments in the global fields. Hence, the total algorithmic derivatives can be computed using the chain rule

$$\mathbb{C}^{uu} = \frac{\partial \boldsymbol{S}}{\partial \boldsymbol{C}} + \frac{\partial \boldsymbol{S}}{\partial \Theta} \frac{\partial \Theta}{\partial \boldsymbol{C}}, \qquad \mathbb{C}^{u\rho} = \frac{\partial \boldsymbol{S}}{\partial \rho} + \frac{\partial \boldsymbol{S}}{\partial \Theta} \frac{\partial \Theta}{\partial \rho}, \qquad \mathbb{C}^{uc} = \frac{\partial \boldsymbol{S}}{\partial c} + \frac{\partial \boldsymbol{S}}{\partial \Theta} \frac{\partial \Theta}{\partial c}. \tag{55}$$

The tangent matrices for the cell density field can also be expanded out

$$\begin{aligned}
\mathbf{K}_{AL}^{\rho u} &= \mathop{\mathbf{A}}_{e=1}^{n_{\mathrm{el}}} \int_{\mathcal{B}_0^e} \Bigg( \left( -2\mathbb{C}^{s_\rho u} \cdot \boldsymbol{F}^T \cdot \nabla_X N_l^e \right) N_a^e \\
&\quad - 2\, \nabla_X N_a^e \cdot \left( \frac{\partial \boldsymbol{C}^{-1}}{\partial \boldsymbol{C}} \cdot \boldsymbol{F}^T \cdot \nabla_X N_l^e \right) \cdot \left( D^{\rho\rho} \nabla_X \rho + \rho D^{\rho c} \nabla_X c \right) \Bigg) \mathrm{dV}, \\
\mathbf{K}_{AL}^{\rho\rho} &= \mathop{\mathbf{A}}_{e=1}^{n_{\mathrm{el}}} \int_{\mathcal{B}_0^e} \left( \left( \frac{1}{\Delta t} - \mathbb{C}^{s_\rho \rho} \right) N_a^e N_l^e - \nabla_X N_a^e \cdot \left( D^{\rho c} \boldsymbol{C}^{-1} \cdot \nabla_X c \right) N_l^e - \nabla_X N_a^e \cdot D^{\rho\rho} \boldsymbol{C}^{-1} \cdot \nabla_X N_l^e \right) \mathrm{dV}, \\
\mathbf{K}_{AL}^{\rho c} &= \mathop{\mathbf{A}}_{e=1}^{n_{\mathrm{el}}} \int_{\mathcal{B}_0^e} \left( -\mathbb{C}^{s_\rho c} N_a^e N_l^e - \nabla_X N_a^e \cdot \rho D^{\rho c} \boldsymbol{C}^{-1} \cdot \nabla_X N_l^e \right) \mathrm{dV}.
\end{aligned} \tag{56}$$

Once more the total algorithmic derivatives, $\mathbb{C}^{s_\rho u}$, $\mathbb{C}^{s_\rho \rho}$, $\mathbb{C}^{s_\rho c}$, need to take into account the dependency of the structural variables on the global fields. Just as in (55), use of the chain rule on the source term yields

$$\mathbb{C}^{s_\rho u} = \frac{\partial S_\rho}{\partial \boldsymbol{C}} + \frac{\partial S_\rho}{\partial \Theta} \frac{\partial \Theta}{\partial \boldsymbol{C}}, \qquad \mathbb{C}^{s_\rho \rho} = \frac{\partial S_\rho}{\partial \rho} + \frac{\partial S_\rho}{\partial \Theta} \frac{\partial \Theta}{\partial \rho}, \qquad \mathbb{C}^{s_\rho c} = \frac{\partial S_\rho}{\partial c} + \frac{\partial S_\rho}{\partial \Theta} \frac{\partial \Theta}{\partial c}. \tag{57}$$

For completeness of the derivation we expand the tangent matrices of the chemical field even though it is analogous to the linearization of the cell density field,

$$\begin{aligned}
\mathbf{K}^{cu}_{AL} &= \overset{n_{\text{el}}}{\underset{e=1}{\mathbf{A}}} \int_{\mathcal{B}^e_0} \left( \left( -2\mathbb{C}^{s_c u} \cdot \boldsymbol{F}^T \cdot \nabla_X N^e_l \right) N^e_a - 2\,\nabla_X N^e_a \cdot \left( \frac{\partial \boldsymbol{C}^{-1}}{\partial \boldsymbol{C}} \cdot \boldsymbol{F}^T \cdot \nabla_X N^e_l \right) \cdot D^{cc} \nabla_X c \right) \mathrm{dV}, \\
\mathbf{K}^{c\rho}_{AL} &= \overset{n_{\text{el}}}{\underset{e=1}{\mathbf{A}}} \int_{\mathcal{B}^e_0} \left( -\mathbb{C}^{s_c \rho} N^e_a N^e_l \right) \mathrm{dV}, \\
\mathbf{K}^{cc}_{AL} &= \overset{n_{\text{el}}}{\underset{e=1}{\mathbf{A}}} \int_{\mathcal{B}^e_0} \left( \left( \frac{1}{\Delta t} - \mathbb{C}^{s_c c} \right) N^e_a N^e_l - \nabla_X N^e_a \cdot \rho D^{cc} \boldsymbol{C}^{-1} \cdot \nabla_X N^e_l \right) \mathrm{dV},
\end{aligned} \tag{58}$$

for which the total algorithmic derivatives $\mathbb{C}^{s_c u}, \mathbb{C}^{s_c \rho}, \mathbb{C}^{s_c c}$ are derived analogously to (57). Lastly, we should emphasize that during the linearization process we have introduced the derivatives $\partial \Theta / \partial \Xi$, of the structural parameters with respect to the global solution variables. However, we still have not shown how can we compute these derivatives. In fact, there is no explicit dependence of $\Theta$ on the global fields $\Xi$. Rather, we have only defined rate dependencies in (51). Therefore we proceed by differentiating the local residuals $\mathbf{R}^{\Theta}$ with respect to the global fields

$$\frac{\partial \mathbf{R}^{\Theta}}{\partial \Theta} \cdot \frac{\partial \Theta}{\partial \Xi} + \frac{\partial \mathbf{R}^{\Theta}}{\partial \Xi} = \mathbf{K}^{\Theta\Theta} \cdot \frac{\partial \Theta}{\partial \Xi} + \frac{\partial \mathbf{R}^{\Theta}}{\partial \Xi} = 0, \tag{59}$$

to obtain a linear system of equations from which we can solve for $\partial \Theta / \partial \Xi$,

$$\frac{\partial \Theta}{\partial \Xi} = -\left( \mathbf{K}^{\Theta\Theta} \right)^{-1} \cdot \frac{\partial \mathbf{R}^{\Theta}}{\partial \Xi}. \tag{60}$$

Summarizing, we consider displacements, cell populations, chemical concentration, and structural variables. We require that the displacements satisfy mechanical equilibrium, and that the biological fields evolve in time according to reaction–diffusion equations. The structural variables behave as local dynamical systems influenced by the global solution fields. Numerically, we solve the global fields with a monolithic finite element implementation. The local dynamical systems are solved at the integration points. We use implicit time stepping schemes, therefore requiring Newton–Raphson iterative algorithms for both the local and global problems. To guarantee quadratic convergence of the finite element solver we consistently linearize the global system. The crucial step during the linearization procedure is computing the derivatives of the structural variables with respect to the global fields. This can be achieved by solving an additional linear system locally at the integration points.

## 3. Results

We explore the capabilities of our model in three stages. First by running examples focused on the behavior and sensitivity of the local remodeling laws holding the global fields fixed. Then we explore single element solutions under constant force and constant displacement boundary conditions. Thirdly we consider examples on larger domains in which we can appreciate the temporal and spatial variations.

### *3.1. Local remodeling*

We hold the global variables fixed, therefore focusing on the idealized time evolution of the structural variables $\Theta$, which takes place locally at an integration point. Namely, we solve only for the residuals in (51). We list the parameter values in Table 2 in the Appendix. The cell capacity of skin is $\rho_{\max} = 10\,000$ cells/mm$^3$ [82]. In response to injury, infiltrating macrophages can release an inflammatory signal with peak concentration on the order of $c_{\max} = 1 \times 10^{-4}$ g/mm$^3$ [83]. Unfortunately, several of the parameters are not directly available from the literature. For example, the time constants for the fiber remodeling are an estimate that takes into consideration an approximate time window in which these events take place [71]. Fiber remodeling in wound healing in pigs has been described from days 7 to 40 [84], showing that fibers in scar tissue tend to be more aligned. It remains a challenging task to conduct comprehensive experiments to accurately determine all of the parameters. However, precisely because of the

Table 1
Sensitivity analysis for the local problem (51). The inputs are the global fields $\boldsymbol{F}$, $\rho$, $c$. We keep the same initial conditions for all cases: $\phi(0) = 0$, $\boldsymbol{a}_0(0) = (1, 0)$, $\kappa(0) = 0.5$, $\lambda_a^p(0) = 1$, $\lambda_s^p(0) = 1$. The abscissa of the plots is time measured in days, the ordinate has no units. The peak chemical concentration is $c_{\max} = 1 \times 10^{-4}$ g/mm$^3$, and the maximum cell density is 10 000 cells/mm$^3$. The parameter values are listed in Table 2.

| Global fields | | | Local parameters | | |
|---|---|---|---|---|---|
| $c$ | $\rho$ | $\boldsymbol{F}$ | $\phi$ | $\angle a_0, \kappa$ | $\theta^p$ |
| 0 | $\rho_{\max}$ | $\begin{pmatrix}1 & 0\\ 0 & 1\end{pmatrix}$ | 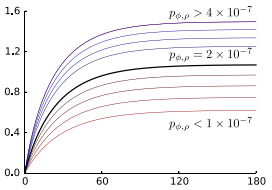  | 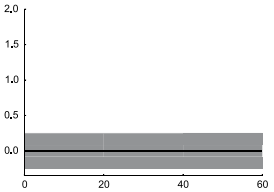 | 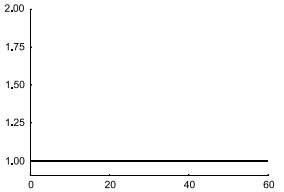 |
| $c_{\max}$ | $\rho_{\max}$ | $\begin{pmatrix}1 & 0\\ 0 & 1\end{pmatrix}$ | 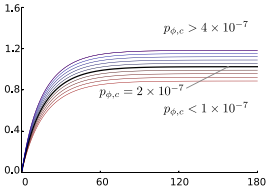  | 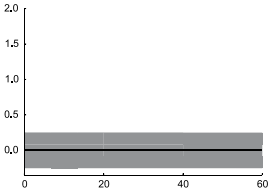 | 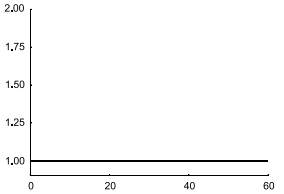 |
| 0 | $\rho_{\max}$ | $\begin{pmatrix}2 & 0\\ 0 & 1\end{pmatrix}$ | 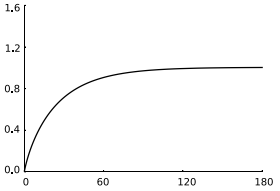 | 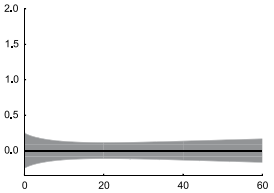 | 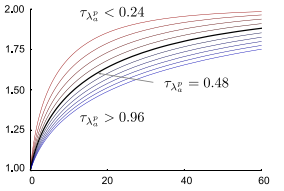  |
| 0 | $\rho_{\max}$ | $\begin{pmatrix}1 & 0\\ 0 & 2\end{pmatrix}$ | 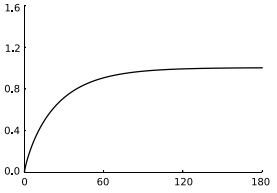 | 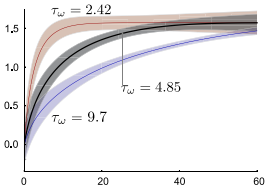  | 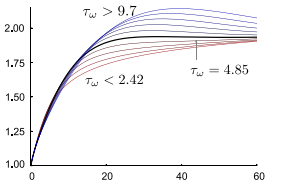  |
| 0 | $\rho_{\max}$ | $\begin{pmatrix}2 & 0\\ 0 & 2\end{pmatrix}$ | 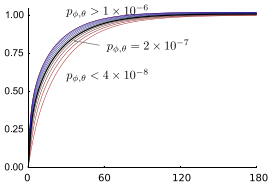  | 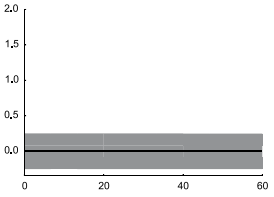 | 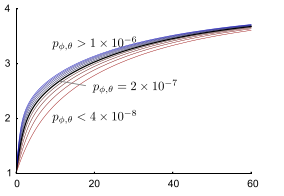  |
| 0 | $\rho_{\max}$ | $\begin{pmatrix}1 & 0.2\\ 0 & 1\end{pmatrix}$ | 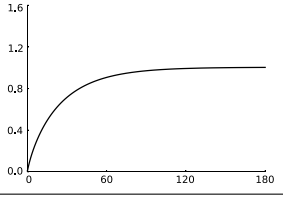 | 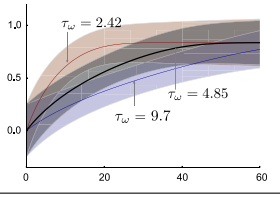  | 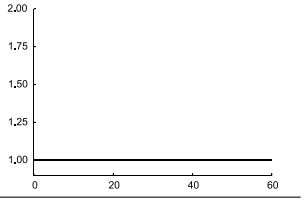 |

uncertainty in the estimation of some of the parameters, it is even more valuable to analyze the behavior of the model under a rich set of conditions.

Table 1 summarizes the tests of different values of $c$, $\rho$ and $\boldsymbol{F}$ as well as sensitivity analysis of some of the parameters. For all the rows in Table 1 the initial conditions are $\phi(0) = 0$, $\boldsymbol{a}_0(0) = (1, 0)$, $\kappa(0) = 0.5$, $\lambda_a^p(0) = 1$, $\lambda_s^p(0) = 1$. The $x$ axis for all the plots is time measured in days. The fourth column plots the collagen fraction. In the fifth column we show the angle of the fiber direction $\boldsymbol{a}_0$ with respect to the basis vector $\boldsymbol{i}_1 = (1, 0)$. The dispersion

is depicted as a thickness around the angle curve, thus, for an isotropic distribution of fibers there is a thickness of $\kappa = 0.5$ along the curve; in contrast, the absence of a shaded area along the angle curve implies perfectly aligned fibers with $\kappa = 0$. The last column shows the permanent area change $\theta^p$. The collagen fraction has been shown to change in wound healing of rats over 180 days, although most of the healing takes place within the first 15–45 days [5,85].

We first test the change in the variables $\Theta$ under no deformation. When the deformation gradient is the identity map there is no reorientation and no change in permanent deformation. The collagen fraction increases monotonically in time. Changing the production rate of the collagen has a noticeable effect on the speed of healing and on the steady state value which can be easily seen in (43) in which $p_{\phi,\rho}$ enters linearly. Similarly, we illustrate the effect of different values of $p_{\phi,c}$ under no deformation (second row in Table 1). More interesting behaviors are captured when the mechanics come into play. Uniaxial stretch along the fiber direction affects the permanent area change in a nonlinear way. Varying the time constants $\tau_{\lambda_a^p}$ and $\tau_{\lambda_s^p}$ produces a family of curves for $\theta^p$, larger values of the time constants lead to slower adaptation. Stretching along the fiber $\boldsymbol{a}_0$ does not induce reorientation, however, it does affect the dispersion $\kappa$. The originally isotropic dispersion decreases initially since the elastic deformation is greater along the $(1, 0)$ direction, then, as the tissue grows in area, the elastic deformation becomes more isotropic and the dispersion increases. Uniaxial stretch orthogonal to the fiber direction induces gradual reorientation. The speed of reorientation is inversely proportional to the parameter $\tau_\omega$. After 60 days the fibers are almost completely aligned in the $(0, 1)$ direction for the entire range of $\tau_\omega$ that we tested (fourth row in Table 1). A biaxial deformation increases the rate of change of $\theta^p$ and also leads to a larger final area gain compared to the uniaxial case (fifth row). For the biaxial test we explore the effect of different values of $p_{\phi,\theta}$, the collagen production rate weighted by the mechanosensing function $\hat{H}(\theta^e + \vartheta^e)$ in (39). The last row in Table 1 shows the effect of pure shear. Since there is no elastic area change $\theta^p$ remains also unchanged, but there is change in the direction $\boldsymbol{a}_0$.

### 3.2. Single element tests

In the previous section no changes in global fields were allowed. Here we consider a single element of dimensions 1 mm × 1 mm. The parameters for the global problem are listed in Table 3 in the Appendix. In the same manner as before, the parameters are either found in the literature or estimated based on experimental observations but in the absence of specific quantitative data. For example, material parameters for the strain energy function used here have been reported elsewhere [67]. In contrast, we did not find parameters for an analytical relation between strain and production of TGF-$\beta$, nonetheless, it has been reported that 10% strain leads to a 2.7-fold increase in TGF-$\beta$ concentration *in vitro* [86], or that strains on the order of 4% and 8% lead to TGF-$\beta$ gene overexpression 2.4 and 3.0-fold higher [45]. We choose 3.3 as the maximum ratio $p_{c,\theta}/p_{c,\rho}$ between strain-induced and autocrine regulation of TGF-$\beta$; however, a more thorough analysis is needed to fit an accurate rate constant.

Our first test is to impose a constant deformation of uniaxial stretch orthogonal to the fiber direction similarly to the cases considered at the integration point level. The initial conditions for the structural variables are also kept as before, $\phi(0) = 0$, $\boldsymbol{a}_0(0) = (1, 0)$, $\kappa(0) = 0.5$, $\lambda_a^p(0) = 1$, $\lambda_s^p(0) = 1$. However, in this case the cell density and the chemical concentration are allowed to change. We investigate the role of different initial conditions for $\rho$ and $c$. Fig. 3 shows the time evolution of $\rho$, $c$, $\phi$, $\angle\boldsymbol{a}_0$ and $\theta^p$ with different values of $\rho(0)$. The initial condition for the chemical is $c(0) = c_{\max}/2$. As expected, the cell density converges to the steady state value $\rho^* = 9000$ cells/mm$^3$ which can be easily computed from (38). The chemical decays exponentially. The remodeling is also faster as the initial cell density increases.

The initial condition for the chemical signal also alters the healing speed. We start with $\rho(0) = 5000$ cells/mm$^3$ and simulate initial concentrations of $c$ ranging from $1 \times 10^{-5}$ to $1 \times 10^{-4}$ g/mm$^3$. The time evolution of the cell density remains unchanged in accordance to what has been reported in the literature [87]. In contrast, larger values of $c(0)$ increase the rate of remodeling (Fig. 4).

More interesting results are achieved when different boundary conditions are imposed on the displacements, allowing for a more preeminent role of the mechanical cues in the remodeling process. The third test of our element leaves the displacements unconstrained and reproduces the permanent contraction of unconstrained collagen gels by fibroblasts [42]. Keeping the initial dispersion $\kappa(0) = 0.5$ leads to a structural tensor $\hat{\boldsymbol{A}} = \boldsymbol{i}_s$, the deformed surface identity. Hence, in this scenario the active stress $\boldsymbol{\sigma}^{\text{act}}$ is proportional to $\boldsymbol{i}_s$ and the gel contracts isotropically. Naturally, he fiber direction remains unchanged and $\kappa = 0.5$ throughout the entire simulation. We do not show those results.

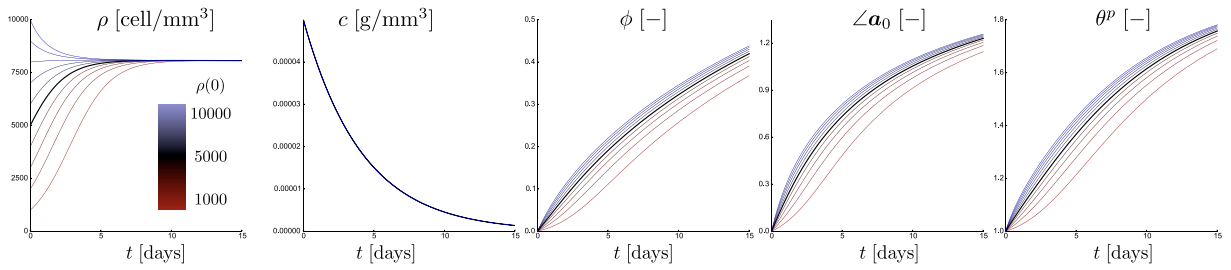


Fig. 3. Single 1 mm × mm element simulation with different initial cell densities $\rho \in [1000, 10\,000]$ cells/mm$^3$ and fixed displacement boundary conditions. The cell density $\rho$ quickly reaches its steady state $\rho^* = 9000$ cells/mm$^3$. The chemical concentration $c$ decays exponentially independently of the initial value of $\rho$. In contrast, the structural variables $\phi$, $\boldsymbol{a}_0$ and $\theta^p = \lambda_a^p \lambda_s^p$ show faster change with higher initial concentrations of $\rho$ during the first 15 days of healing.

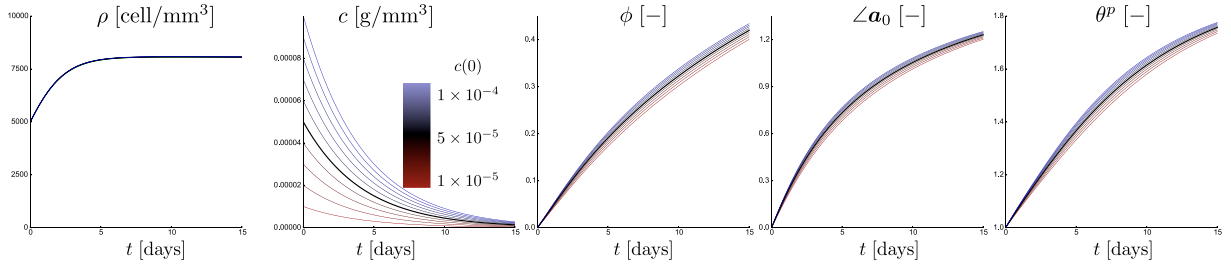


Fig. 4. Single 1 mm × mm element simulation with different initial chemical concentration $c \in [1\times10^{-5}, 1\times10^{-4}]$ g/mm$^3$ and fixed displacement boundary conditions. The cell density $\rho$ quickly reaches its steady state $\rho^* = 9000$ cells/mm$^3$ independently of the initial value of $c$. The chemical concentration $c$ decays exponentially. Since $c$ is associated with the up-regulation of collagen deposition, higher initial concentrations of $c$ are reflected in faster remodeling for the structural variables $\phi$, $\boldsymbol{a}_0$ and $\theta^p = \lambda_a^p \lambda_s^p$ during the first 15 days of healing.

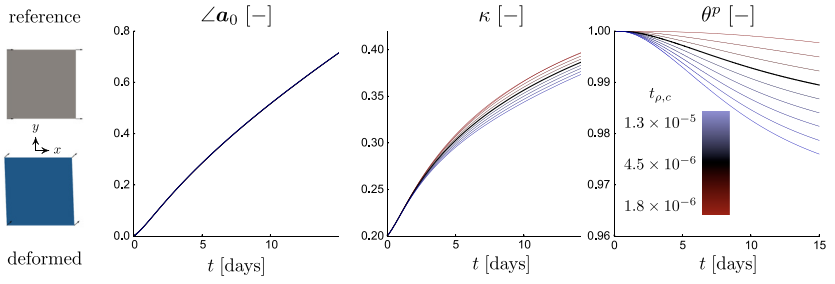


Fig. 5. Single 1 mm × mm element simulation to capture tissue contracture. The lower left node is fixed while the lower right node is constrained in the $y$ direction. The initial fiber direction is $\boldsymbol{a}_0 = (1, 0)$ with dispersion $\kappa = 0.25$. Active stress generated by the cell population causes an elastic deformation, however, as time progresses, the deformation becomes permanent and $\theta^p$ decreases over time. The contraction in the $x$ direction leads to reorientation of $\boldsymbol{a}_0$ and to change in dispersion $\kappa$. The initial and deformed configurations of the element at the end of 15 days are also depicted.

To showcase a more unusual response we change the initial dispersion to $\kappa = 0.25$. The fiber orientation $\boldsymbol{a}_0$ defines a structural tensor $\hat{\boldsymbol{A}} \neq \boldsymbol{i}_s$. The active stress exerted by the fibroblasts in this setting is anisotropic and weights more the $(1, 0)$ direction. We illustrate the result in Fig. 5. For our element, the lower left node is fixed and the lower right corner is constrained in the $y$ direction. Active stress generated by the cell density field initially contracts the tissue elastically in the $x$ axis. At the same time, since the principal direction of the elastic component of $\boldsymbol{C}^e$ is aligned with the $y$ axis, there is reorientation of $\boldsymbol{a}_0$. Then, as $\phi$ increases the elastic deformation becomes gradually fixed and $\theta^b$ decreases over time. We explore different values for $t_{\rho,c}$, the contractile stress associated with fibroblasts in the presence of TFG-$\beta$. Larger values of $t_{\rho,c}$ result in greater contracture or, equivalently, smaller area at the end of $t = 15$ days.

### 3.3. Spatiotemporal evolution of wound healing

We turn our attention to a more realistic domain. We consider a square of tissue of dimensions $\Omega := 100$ mm $\times$ 100 mm. We discretize the geometry with $35 \times 35$ elements. We fix the displacements along the boundary $\partial\Omega$. We also impose Dirichlet boundary conditions for the biological fields, setting $\rho_{\partial\Omega} = 9000$ cells/mm$^3$ and $c_{\partial\Omega} = 0.0$ g/mm$^3$. We create a circular wound of 20 mm in diameter at the center of the domain. The wound tissue lacks collagen and fibroblasts; instead, at the beginning of the proliferation phase, the wound is filled with granulation tissue and inflammatory chemokines [3]. Therefore we define the wound the initial conditions as $\rho_{\text{wound}}(0) = 0$, $c_{\text{wound}}(0) = 1 \times 10^{-4}$, $\phi_{\text{wound}}(0) = 0$, $\kappa_{\text{wound}}(0) = 0.5$, $\lambda^p_{a,\text{wound}}(0) = 1$, $\lambda^p_{s,\text{wound}}(0) = 1$. The fiber direction in the wound, $\boldsymbol{a}_{0,\text{wound}}(0)$ is initialized with random directions. The healthy tissue is characterized by the presence of collagen in a preferred orientation, cells, and lack of inflammation, consequently, for the healthy tissue we choose initial conditions $\rho_{\text{health}}(0) = 9000$, $c_{\text{health}}(0) = 0.0$, $\phi_{\text{health}}(0) = 1.0$, $\boldsymbol{a}_{0,\text{health}}(0) = (1, 0)$, $\kappa_{\text{health}}(0) = 0.25$, $\lambda^p_{a,\text{health}}(0) = 1$, $\lambda^p_{s,\text{health}}(0) = 1$. Instead of using an exact Heaviside function to separate the healthy and wounded subdomains we create a narrow transition region between the wound domain and the healthy tissue. Fig. 6 summarizes the results of the simulation. The columns, from left to right, show different time points $t = 0, 3.75, 7.7, 11.25, 15$ days. The contours of the cell density field $\rho$ show how infiltration of the cells into the wound is relatively fast and by day $t = 3.75$ the value of $\rho$ inside the wound averages 9078 cells/mm$^3$ (first row in Fig. 6). The chemical concentration contours illustrate diffusion and exponential decay of the chemical concentration field (second row). By the end of the simulation at $t = 15$ days, $c$ averages $1 \times 10^{-6}$ g/mm$^3$ inside of the wounded region. The recovery of the collagen content field $\phi$ is slower compared to the time evolution of $\rho$ and $c$. By the end of the simulation the average value is $\phi = 0.42$ at the center. Recall that the active stress $\boldsymbol{\sigma}^{\text{act}}$ is a function of $c$, $\rho$, $\phi$, and $\boldsymbol{a}_0$. Therefore the wound domain itself is not contracted initially as it lacks collagen and cells, rather, contraction of the wound occurs because skin deforms primarily in an annular region surrounding the wound in agreement with experimental observations [82]. As time progresses, collagen deposition by fibroblasts turns the elastic deformation into a permanent contracture (bottom row in Fig. 6).

With a finite element implementation it is possible to explore the effects of different initial wound geometries. One important consideration in clinical practice comes from the fact that wounds produce different scar and contraction depending on the initial orientation of the wound with respect to that of the collagen fibers in the dermis [88]. In the model presented here and based on the literature [48], the myofibroblasts which are the cells associated to contracture, exert tractions primarily along the fiber direction. Our simulations show that an elliptical wound of ratio 1:2, oriented orthogonal to the fibers leads to a increased contracture compared to an elliptical wound with ratio 2:1 oriented parallel to the fiber direction $\boldsymbol{a}_0$ (third column in Fig. 7). The collagen deposition is similar in both elliptic wounds and it is also comparable to the circular wound. The elliptical wound with parallel orientation averaged $\phi = 0.41$ in the center region of the wound, the elliptical wound of ratio 1:2 averaged $\phi = 0.41$ as well.

In Fig. 8 we show the change in fiber direction at 15 days compared to the initial state $t = 0$. To define the wounds we initialized the fibers in the wound domain with random orientations and isotropic dispersion $\kappa = 0.5$, see Fig. 8 top row. At the end of $t = 15$ days the fibers are not fully aligned, yet the average direction in the wounded region is $\boldsymbol{a}_0 = (0.753, 0.658)$ for the circular geometry, $\boldsymbol{a}_0 = (0.775, 0.631)$ for the 2:1 ellipse, and $\boldsymbol{a}_0 = (0.81, 0.58)$ for the 1:2 ellipse. Interestingly, the fibers in the annular region surrounding the wounded domain, which were originally perfectly aligned in the $(1, 0)$ direction, contribute to the reorientation as a result of contraction. This is in agreement with our single element tests. Experimental characterization of human scar tissue has shown that collagen fibers are thinner and more aligned in scars compared to healthy tissue [47]. Experiments in rats have shown the presence of whorl-like structures in the transition region between healthy and scar tissue suggesting a transition in the direction of the fibers from the healthy tissue towards the alignment in the wounded area [89]. However, it remains challenging to make quantitative comparisons to our simulations. Moreover, given that our model relies on the alignment of fibers to the principal stretch components, the notion of anisotropic prestrain is of primary importance [90], but we did not test that aspect in the simulations we present here.

## 4. Discussion

Living tissues are characterized by a strong coupling between microstructure, cell populations, chemical cell-signaling, and mechanical loads. Here we present a novel framework for modeling the adaptation of biological

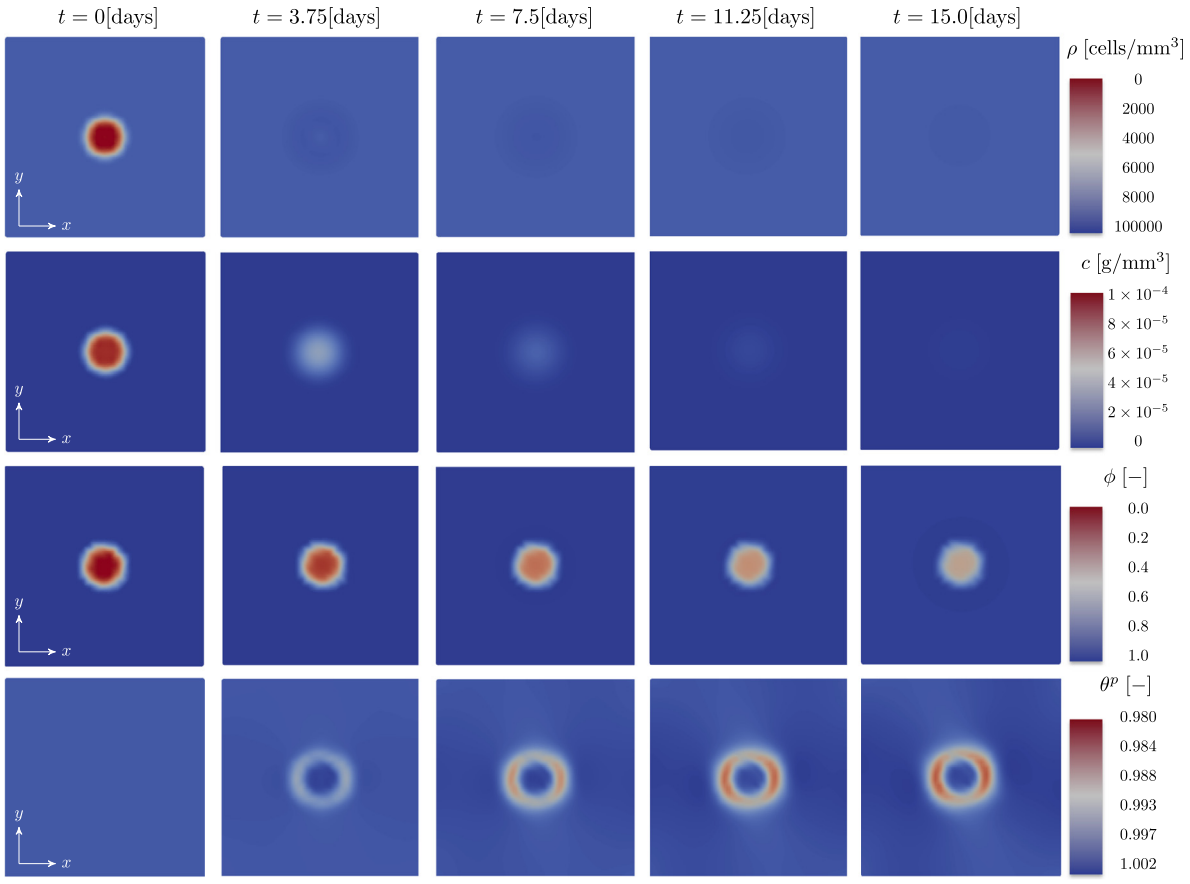


Fig. 6. Spatiotemporal evolution of the healing of a circular wound of 20 mm diameter in a $100 \times 100$ mm$^2$ domain during the first 15 days of healing. The columns are snapshots at different time points. The initial condition defining the wound is the absence of cells and collagen, and a peak chemical concentration. Contours of $\rho$ show how the fibroblast population quickly fills the wounded domain, first row. The chemical signal, second row, diffuses and degrades such that by the end of the simulation the value at the center averages $1 \times 10^{-6}$ g/mm$^3$. The production of collagen, third row, is much slower, by day $t = 15$ the collagen fraction at the center averages 0.42. The last row shows the permanent area change of the tissue. Since active contraction depends on the fiber alignment $\boldsymbol{a}_0$, the presence of collagen $\phi$, and the chemical concentration $c$, contracture is localized in a ring surrounding the wound.

systems that brings together developments in mechanics of growth and remodeling with systems biology descriptions. This work is the continuation of a previously published manuscript by the author and coworkers [34]. In our initial efforts we introduced the concept of coupled chemo-bio-mechanical systems, but we restricted our attention to a simple coupling between mechanics and biology through the change in mass fractions of the tissue constituents. Here, in addition to a refinement of the constitutive equations and couplings, we introduce a more general remodeling approach for the microstructure. In addition to mass fractions of the tissue constituents, we consider geometric entities such as fiber remodeling and permanent volume changes. We discretize the resulting equations with finite elements, solving globally for the displacement fields, the cell densities, and the chemical signals; and locally for the changes in microstructure. The resulting model and numerical algorithm allow to recapitulate the systems mechanobiology of wound healing. We showcased simulations at the integration point, the element level, and a sizable patch of skin tissue. While this work is focused primarily on cutaneous wound healing, the theoretical and computational framework is applicable to many other similar processes of mechanical adaptation in mammalian tissues [18], and it will hopefully continue to enable new discussions between scientists working at the crossroads of computational biomechanics and systems biology.

Connective tissues such as skin have evident mechanical roles which are crucial for survival and optimal physiological function. Our interaction with the world requires a variety of forces and deformations transmitted through our skin. Therefore, to guarantee homeostasis and proper mechanical function, cutaneous cell populations

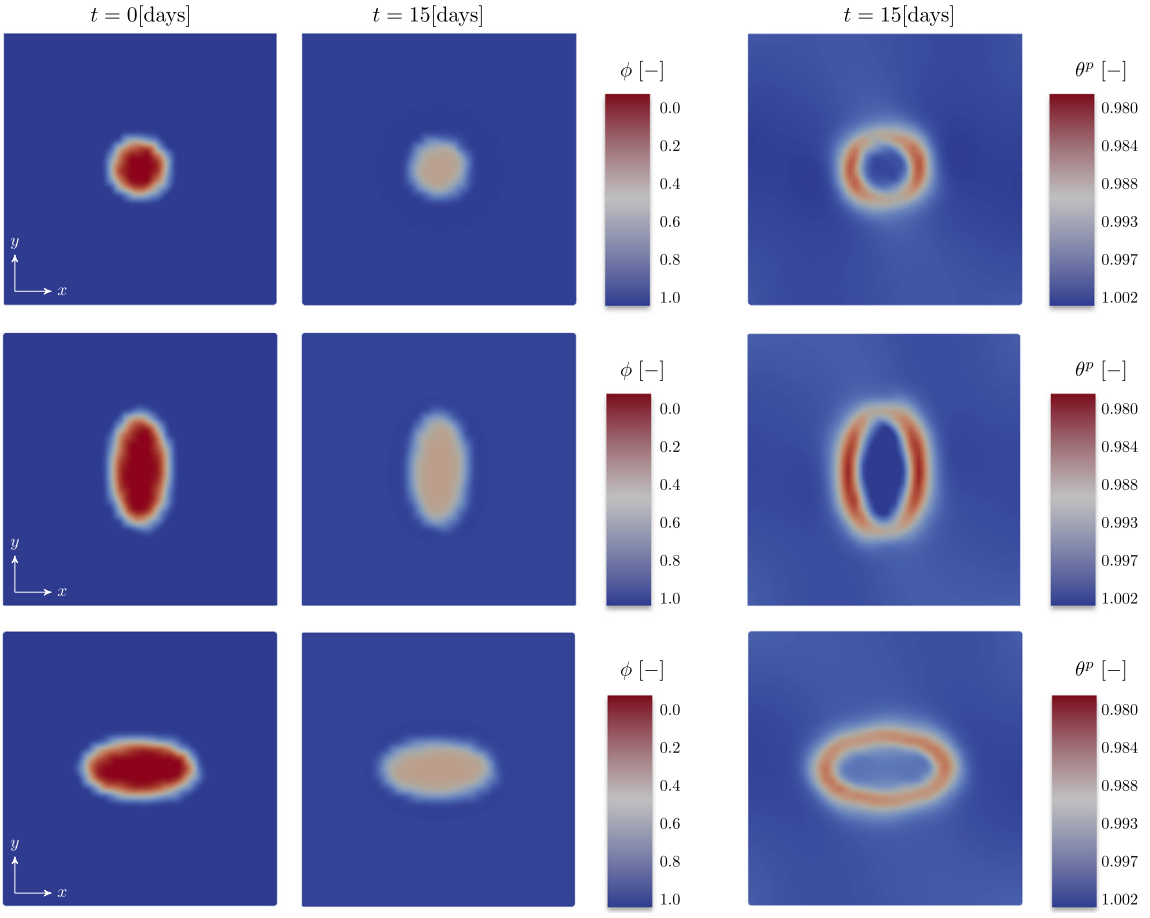


Fig. 7. Differences in collagen deposition $\phi$ and permanent contracture $\theta^p$ of wounds with different ellipticity and orientation. The wound is initialized by setting $\phi = 0$ in a subset of the domain, left column. We explore a circular geometry, an ellipse with ratio 1:2 oriented orthogonal to the initial fiber direction $\boldsymbol{a}_0$, and an elliptical wound of ratio 2:1. By $t = 15$ days the collagen content averages $\phi = 0.42$ in the circular wound, and $\phi = 0.41$ in both elliptical wounds, middle column. Permanent area contours show the most significant variation. A wound oriented orthogonal to the initial fiber alignment results in greater contracture, right column.

have to be able to respond to mechanical cues and regenerate the tissue upon injury [91]. Mechanical adaptation of biological systems commonly involves an orchestra of cells and their various signaling pathways [19]. Experimental data alone is not enough to dissect the mechanisms governing the tissue regeneration process [52]. Current experimental techniques in biology are becoming powerful tools that produce massive amounts of data. Perhaps the most preeminent example is genomics, which is paving the way for personalized medicine [92]. Yet, it has also been emphasized that characterizing the genome alone is insufficient. The response of living systems to different stimuli is the result of a complex network of interactions that span several spatial and temporal scales; mechanical form and function emerge from the dynamics of such networks [19]. Therefore we need to propose and validate mathematical descriptions of how the parts connect to each other and evolve synchronously in space and time. In particular, mechanical forces and deformations play a central role in several clinical scenarios. Computational systems mechanobiology aims at building the modeling and simulation tools to understand the mechanical form and function of soft tissues in health and disease by explicitly taking into account cells as the leading actors in the mechanical adaptation events together with their signaling networks.

In this work the focus is on cutaneous wound healing. Skin is a thin transversely isotropic membrane with nonlinear mechanical response governed by the presence of a collagen network. We describe the mechanical behavior of skin with a strain energy function that incorporates the collagen content, the preferred fiber alignment, and the fiber dispersion. We incorporate the split of the deformation gradient into biologic and elastic contributions. The split of the

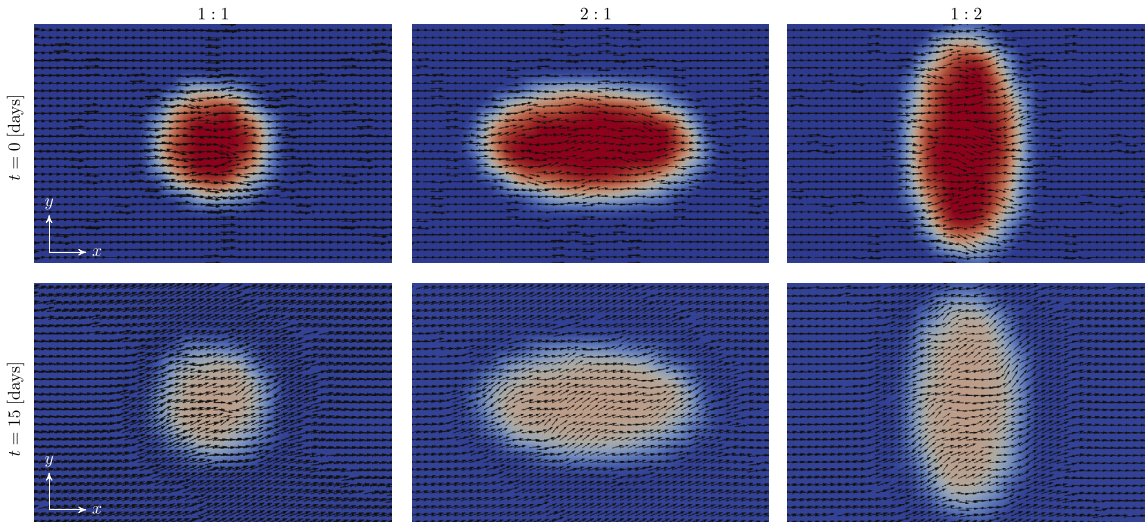


Fig. 8. Comparison of fiber reorientation during wound healing in different geometries. In all cases the initial condition for the fiber direction $\boldsymbol{a}_0$ inside of the wound is random, while the surrounding healthy tissue is perfectly aligned $\boldsymbol{a} = (1, 0)$. The fiber orientation in the circular geometry $1:1$ averages $\boldsymbol{a}_0 = 0.753, 0.658$ at $t = 15$ days. The 2:1 wound leads to fibers with mean orientation $\boldsymbol{a}_0 = (0.775, 0.631)$ while for the 1:2 ellipse the value is $\boldsymbol{a}_0 = (0.81, 0.58)$.

deformation gradient has been used to model growth in living tissues [24]. We avoid the term *growth* because in wound healing the term *contracture* is commonly used to denote the permanent shrinkage of the tissue [60]. At the same time, the model we propose can also account for growth and not only contracture, hence our decision to simply distinguish between elastic and biologic contributions. Following the split, the elastic response of the tissue is determined with respect to the intermediate configuration which is in turn defined by the permanent volume change and the changes in collagen content, fiber alignment, and fiber dispersion. Instead of proposing purely phenomenological constitutive laws to capture the remodeling process, we explicitly consider a cell population density field as the leading actor. This scalar field represents the fibroblast and myofibroblast cell populations that are in charge of regenerating the dermis during wound healing. The cell activity consists of migration, proliferation, production of chemical signals, collagen deposition, and active contraction of the tissue. Even though the healing process involves several chemical substances we consider a single scalar field that lumps together the action of some of these chemokines with a stronger emphasis on TGF-$\beta$. The spatiotemporal evolution of the cell density field and the chemical signal is governed by a reaction–diffusion system of partial differential equations. However, as we have pointed out, there is a local coupling between the cellular activity and the remodeling process. Namely, as the cells deform the tissue and lay down new collagen, they effectively drive the change in volume, fiber direction, and fiber dispersion which we had not taken into consideration before yet it has been observed in experiments [34,82]. The feedback loop is closed by introducing a mechanotransduction term that was also lacking in our earlier work [34]. Mechanotransduction is the mechanism by which cells sense the local state of deformation [44]. In skin, fibroblast mechanotransduction leads to production of TGF-$\beta$ and collagen deposition by fibroblasts.

Simulations at the integration point level show how collagen production is proportional to the cell density and the chemical concentration. When a deformation gradient is imposed, the fiber direction changes to align with the principal stretch and the tissue area changes permanently as new collagen is being deposited. The integration point simulations can be related to experimental design focused on the basic mechanisms of cellular activity and its effect on the local microstructure, for example in the determination of forces exerted by fibroblasts on different substrates [15]. The single element simulations can be the equivalent to controlled experiments in which one could expect homogeneous samples such as uniform gel contraction experiments [42]. The greatest potential of the model is, however, the full domain simulation. We show how different initial wound geometries evolve over the same span of fifteen days. The active stress imposed by the cell population depends on the collagen content, fiber alignment, and the chemical signal; thus, the wound contracts primarily in a ring in the periphery of the disrupted tissue, a fact that has been acknowledge and discussed in the literature [93,82]. To highlight the effects of anisotropy, we show the

Table 2
Parameters used for the local problem defined by (51).

| Parameter | Value/Range | Interpretation |
|---|---|---|
| $p_\phi$ | $2 \times 10^{-7}$ [1/h] | Physiological rate of collagen deposition [95] |
| $p_{\phi c}$ | $2 \times 10^{-7}$ [1/h] | Collagen production rate activated by chemokine [85] |
| $p_{\phi\theta}$ | $2 \times 10^{-7}$ [1/h] | Collagen production rate activated by stretch |
| $K_{\phi c}$ | 0.0001 [−] | Saturation of the effect of the chemokine in the collagen production rate |
| $K_{\phi\rho}$ | 1.06 [−] | Saturation of collagen production by increasing collagen fraction |
| $d_\phi$ | 0.00097 [1/h] | Collagen degradation [95] |
| $d_{\phi,c}$ | 0.000485 [1/h] | Enhanced collagen degradation in the presence of an inflammatory signal [95] |
| $\tau_\omega$ | 4.85 [h] | Time constant for fiber reorientation |
| $\tau_\kappa$ | 0.485 [h] | Time constant for fiber dispersion remodeling |
| $\gamma_\kappa$ | 2 [−] | Shape of dispersion rate curve |
| $\tau_{\lambda_a^p}$ | 0.485 [h] | Time constant for the rate of permanent deformation |
| $\tau_{\lambda_s^p}$ | 0.485 [h] | Time constant for the rate of permanent deformation |
| $\gamma_\theta$ | 5 [−] | Shape of mechanosensing curve |
| $\vartheta^e$ | 2 [−] | Midpoint of $\hat{H}$ [96] |

Table 3
Parameters used for the global problem defined by (50).

| Parameter | Value/Range | Interpretation |
|---|---|---|
| $k_0$ | 0.0511 [Mpa] | Passive material response [67] |
| $k_f$ | 0.015 [MPa] | Collagen stiffness [67] |
| $k_2$ | 0.048 [−] | Passive material response [67] |
| $t_\rho$ | $4.5 \times 10^{-6}$ [MPa] | Active stress by myofibroblasts [97] |
| $t_{\rho,c}$ | $4.5 \times 10^{-6}$ [MPa] | Up-regulation of contraction by the presence of a chemokine [42] |
| $K_{\tau,c}$ | $1 \times 10^{-5}$ [−] | Saturation of the cellular response to the chemokine |
| $D^{\rho,\rho}$ | 0.0833 [$mm^2$/h] | Cell diffusion [98] |
| $D^{\rho,c}$ | $1.66 \times 10^{-4}$ [$mm^5$/g h] | Cell chemotaxis [85] |
| $D^{cc}$ | 0.10 [$mm^2$/ h] | Diffusion constant for chemical [99] |
| $p_\rho$ | 0.034 [1/h] | Proliferation rate of fibroblasts [85] |
| $p_{\rho,c}$ | 0.001 [1/h] | Enhanced proliferation of fibroblasts [87] |
| $K_{\rho,c}$ | $1 \times 10^{-5}$ [−] | Saturation of cellular response to the chemokine |
| $d_\rho$ | 0.0068 [1/h] | Fibroblast apoptosis rate |
| $K_{\rho,\rho}$ | 10 000 [−] | Tissue cell capacity [98] |
| $p_{c,\rho}$ | $9 \times 10^{-19}$ [1/h] | Positive feedback of chemical production by cells |
| $p_{c,\theta}$ | $3 \times 10^{-18}$ [1/h] | Positive feedback of chemical production in response to stretch |
| $K_{c,c}$ | $9 \times 10^{-12}$ [−] | Saturation shape of the chemical production rate |
| $d_c$ | 0.01 [1/h] | Decay of the chemical [98] |

difference in the healing of an elliptical wound when it is placed parallel or orthogonal to the fiber direction. Since the active stress reflects the fiber alignment, wounds oriented orthogonal to the fiber direction have a higher degree of permanent area change. One limitation of our work is the need for calibration in order to make the model relevant for the bioengineering community. The mechanical properties of skin tissues and the architecture of the collagen network in healthy skin have been studied extensively [36]. Wound healing studies have focused on the ultimate strength of the tissue rather than detailed stress–strain relations and how these evolve in time. Furthermore, there is a need to quantify the special variations in collagen morphology and anisotropy during healing and not just at the center of the wound [5,47]. From the biological point of view, the signaling network has been thoroughly described, yet, few quantitative rate parameters have been measured. To address this limitation one possible strategy is to monitor the spatial and temporal variation of chemokine concentration and gene expression similar to [94] where the focus was on the spatiotemporal dynamics of inflammatory signaling in mice wounds.

In conclusion, the model presented is a step forward towards a better understanding of the integration between mechanics and biology [34]. We describe coupled chemo-bio-mechanical systems starting from a continuum mechanics description and explicitly incorporate cellular and chemical fields which are coupled locally to drive

the growth and remodeling processes. We show the numerical implementation of our model with a finite element formulation. The focus of our study is the systems mechanobiology of wound healing, however, many processes of mechanical adaptation in biological systems obey a similar structure, although with different cell types, chemical signals, and specific couplings between them. Future tasks include extension to three dimensional membranes, and experimental efforts for validation and calibration. Nevertheless, we hope that our contribution will serve as a step towards better understanding of the dynamical adaptation of living tissues with the ultimate goal of becoming predictive computational tools that could be used in clinical practice and medical device design.

## Appendix

See Tables 2 and 3.

## References

[1] A.J. Singer, R.A. Clark, Cutaneous wound healing, New Engl. J. Med. 341 (10) (1999) 738–746.
[2] P. Martin, Wound healing: aiming for perfect skin regeneration, Science 276 (1997) 75–81.
[3] G.C. Gurtner, S. Werner, Y. Barrandon, M.T. Longaker, Wound repair and regeneration, Nature 453 (2008) 314–321.
[4] B.J. Larson, M.T. Longaker, H.P. Lorenz, Scarless fetal wound healing: a basic science review, Plast. Reconstr. Surg. 126 (4) (2010) 1172–1180.
[5] C.J. Doillon, M.G. Dunn, E. Bender, F.H. Silver, Collagen fiber formation in repair tissue: development of strength and toughness, Collagen Relat. Res. 5 (6) (1985) 481–492.
[6] L. Van De Water, S. Varney, J.J. Tomasek, Mechanoregulation of the myofibroblast in wound contraction, scarring, and fibrosis: opportunities for new therapeutic intervention, Adv. Wound Care 2 (4) (2013) 122–141.
[7] A. Buganza Tepole, E. Kuhl, Review: Systems-based approaches towards wound healing, Pediatr. Res. 73 (2013) 553–563.
[8] S. Schreml, R.M. Szeimies, L. Prantl, M. Landthaler, P. Babilas, Wound healing in the 21st century, J. Am. Acad. Dermatol. 63 (5) (2010) 866–881.
[9] S. Enoch, D.J. Leaper, Basic science of wound healing, Surgery (Oxford) 26 (2) (2008) 31–37.
[10] N.T. Bennett, G.S. Schultz, Growth factors and wound healing: biochemical properties of growth factors and their receptors, Am. J. Surg. 165 (6) (1993) 728–737.
[11] T.J. Carrico, A.I. Mehrhof Jr., I.K. Cohen, Biology of wound healing, Surg. Clin. North Am. 64 (4) (1984) 721–733.
[12] K. Safferling, T. Sutterlin, K. Westphal, C. Ernst, K. Breuhahn, M. James, D. Jager, N. Halama, N. Grabe, Wound healing revised: a novel reepithelialization mechanism revealed by in vitro and in silico models, J. Cell Biol. 203 (4) (2013) 691–709.
[13] A.A. Qutub, F.M. Gabhann, E.D. Karagiannis, P. Vempati, A.S. Popel, Multiscale models of angiogenesis, IEEE Eng. Med. Biol. Mag. 28 (2) (2009) 14–31.
[14] S. Werner, T. Krieg, H. Smola, Keratinocyte-fibroblast interactions in wound healing, J. Invest. Dermatol. 127 (5) (2007) 998–1008.
[15] B. Li, J.H.C. Wang, Fibroblasts and myofibroblasts in wound healing: force generation and measurement, J. Tissue Viability 20 (4) (2001) 108–120.
[16] J.J. Tomasek, G. Gabbiani, B. Hinz, C. Chaponnier, R.A. Brown, Myofibroblasts and mechano-regulation of connective tissue remodelling, Nat. Rev. Mol. Cell Biol. 3 (5) (2002) 349–363.
[17] H. Kitano, Computational systems biology, Nature 420 (2002) 206–210.
[18] Y. Vodovotz, M. Csete, J. Bartels, S. Chang, G. An, Translational systems biology of inflammation, PLoS Comput. Biol. 4 (2008) e1000014.
[19] V.W. Wong, S. Akaishi, M.T. Longaker, G.C. Gurtner, Pushing back: wound mechanotransduction in repair and regeneration, J. Invest. Dermatol. 131 (11) (2011) 2186–2196.
[20] C.Y. Hui, L. Rong, A constitutive model for the large deformation of a self-healing gel, Soft Matter 8 (31) (2012) 8209–8216.
[21] G.A. Holzapfel, T.C. Gasser, R.W. Ogden, A new constitutive framework for arterial wall mechanics and a comparative study of material models, J. Elasticity 61 (2000) 1–48; Comput. Methods Appl. Mech. Engrg. 132 (1996) 45–61.
[22] M. Eskandari, E. Kuhl, Systems biology and mechanics of growth, WIREs Syst. Biol. Med. 7 (2015) 401–412.
[23] B. Baillargeon, N. Rebelo, D.D. Fox, R.L. Taylor, E. Kuhl, The living heart project: A robust and integrative simulator for human heart function, Eur. J. Mech. A Solids 48 (2014) 38–47.
[24] D. Ambrosi, G.A. Ateshian, E.M. Arruda, S.C. Cowin, J. Dumais, A. Goriely, G.A. Holzapfel, J.D. Humphrey, R. Kemkemer, E. Kuhl, J.E. Olberding, L.A. Taber, K. Garikipati, Perspectives on biological growth and remodeling, J. Mech. Phys. Solids 59 (2011) 863–883.
[25] A. Menzel, A fibre reorientation model for orthotropic multiplicative growth, Biomech. Model. Mechanobiol. 6 (2007) 303–320.
[26] C.A. Figueroa, S. Baekb, C.A. Taylor, J.D. Humphrey, A computational framework for fluid-solid-growth modeling in cardiovascular simulations, Comput. Methods Appl. Mech. Engrg. 198 (2009) 3583–3602.
[27] S. Scheiner, P. Pivonka, C. Hellmich, Coupling systems biology with multiscale mechanics, for computer simulations of bone remodeling, Comput. Methods Appl. Mech. Engrg. 254 (2013) 181–196.
[28] D.E. Moulton, A. Goriely, R. Chirat, Mechanical growth and morphogenesis of seashells, J. Theoret. Biol. 311 (2012) 69–79.
[29] T. Waffenschmidt, A. Menzel, E. Kuhl, Anisotropic density growth of bone- a computational micro-sphere approach, Int. J. Solids Struct. 49 (14) (2012) 1928–1946.
[30] S. Budday, P. Steinmann, E. Kuhl, The role of mechanics during brain development, J. Mech. Phys. Solids 72 (2014) 75–92.

[31] C. Valero, E. Javierre, J.M. Garcia-Aznar, A. Menzel, MJ. Gomez-Benito, Challenges in the modeling of wound healing mechanisms in soft biological tissues, Ann. Biomed. Eng. 43 (7) (2015) 1654–1665.
[32] E. Kuhl, G.A. Holzapfel, A continuum model for remodeling in living structures, J. Mater. Sci. 42 (2007) 8811–8823.
[33] M. Holcombe, S. Adra, M. Bicak, S. Chin, S. Coakley, A.I. Graham, J. Green, C. Greenough, D. Jackson, M. Kiran, S. MacNeil, A. Maleki-Dizaji, P. McMinn, M. Pogson, R. Poole, E. Qwarnstrom, F. Ratnieks, M.D. Rolfe, R. Smallwood, T. Sun, D. Worth, Modelling complex biological systems using an agent-based approach, Integr. Biol. 4 (1) (2012) 53–64.
[34] A. Buganza Tepole, E. Kuhl, Computational modeling of chemo-bio-mechanical coupling: A systems-biology approach towards wound healing. Comput. Methods Biomech. Biomed. Eng.. http://dx.doi.org/10.1080/10255842.2014.980821.
[35] C.L. Simpson, D.M. Patel, K.J. Green, Deconstructing the skin: cytoarchitectural determinants of epidermal morphogenesis, Nat. Rev. Mol. Cell Biol. 12 (9) (2011) 565–580.
[36] J.W.Y. Jor, M.D. Parker, A.J. Taberner, M.P. Nash, P.M.F. Nielsen, Computational and experimental characterization of skin mechanics: Identifying current challenges and future directions, Wiley Interdiscip. Rev.: Syst. Biol. Med. 5 (2013) 539–556.
[37] S.A. Eming, T. Krieg, J.M. Davidson, Inflammation in wound repair: molecular and cellular mechanisms, J. Invest. Dermatol. 127 (3) (2007) 514–525.
[38] A.E. Postlethwaite, J. Keski-Oja, H.L. Moses, A.H. Kang, Stimulation of the chemotactic migration of human fibroblasts by transforming growth factor beta, J. Exp. Med. 165 (1) (1987) 251–256.
[39] G.S. Schultz, A. Wysocki, Interactions between extracellular matrix and growth factors in wound healing, Wound Repair Regen 17 (2) (2009) 153–162.
[40] G.R. Grotendorst, H. Rahmanie, M. Duncan, Combinatorial signaling pathways determine fibroblast proliferation and myofibroblast differentiation, FASEB 18 (2004) 469–479.
[41] B. Hinz, The myofibroblast: Paradigm for a mechanically active cell, J. Biomech. 43 (2010) 146–155.
[42] R. Montesano, L. Orci, Transforming growth factor beta stimulates collagen-matrix contraction by fibroblasts: implications for wound healing, Proc. Natl. Acad. Sci. 85 (13) (1988) 4894–4897.
[43] H. Hatami-Marbini, M.R. Mofrad, Cytoskeletal mechanics and cellular mechanotransduction: a molecular perspective, in: Cellular and Biomolecular Mechanics and Mechanobiology, Springer, Berlin, Heidelberg, 2011, pp. 3–27.
[44] J.H.C. Wang, B.P. Thampatty, J.S. Lin, H.J. Im, Mechanoregulation of gene expression in fibroblasts, Gene 391 (2007) 1–15.
[45] C. Jiang, L. Shao, Q. Wang, Y. Dong, Repetitive mechanical stretching modulates transforming growth factor-beta induced collagen synthesis and apoptosis in human patellar tendon fibroblasts, Biochem. Cell Biol. 90 (5) (2012) 667–674.
[46] S.M. Levenson, E.F. Geever, L.V. Crowley, J.F. Oates III, C.W. Berard, H. Rosen, Healing of rat skin wounds, Ann. Surg. 161 (2) (1965) 293.
[47] C.A. Grant, P.C. Twigg, D.J. Tobin, Static and dynamic nanomechanical properties of human skin tissue using atomic force microscopy: effect of scarring in the upper dermis, Acta Biomater. 8 (11) (2012) 4123–4129.
[48] S. Loerakker, C. Obbink-Huizer, FPT. Baaijens, A physically motivated constitutive model for cell-mediated compaction and collagen remodeling in soft tissues, Biomech. Model. Mechanobiol. 13 (2014) 985–1001.
[49] E. Javierre, P. Moreno, M. Doblare, J.M. Garcia-Aznar, Numerical modeling of a mechano-chemical theory for wound contraction analysis, Int. J. Solids Struct. 46 (2009) 3597–3606.
[50] P. Cermelli, M.E. Gurtin, On the characterization of geometrically necessary dislocations in finite plasticity, J. Mech. Phys. Solids 49 (7) (2001) 1539–1568.
[51] F. Baaijens, C. Bouten, N. Driessen, Modeling collagen remodeling, J. Biomech. 43 (1) (2010) 166–175.
[52] D. Noble, The rise of computational biology, Nat. Rev. Mol. Cell Biol. 3 (6) (2002) 459–463.
[53] H. Dal, S. Goktepe, M. Kaliske, Kuhl, A fully implicit finite element method for bidomain models of cardiac electromechanics, Comput. Methods Appl. Mech. Engrg. 253 (1) (2013) 323–336.
[54] G. Himpel, E. Kuhl, A. Menzel, P. Steinmann, Computational modelling of isotropic multiplicative growth, CMES Comput. Model. Eng. Sci. 8 (2005) 119–134.
[55] M.K. Rausch, E. Kuhl, On the mechanics of growing thin biological membranes, J. Mech. Phys. Solids 63 (2014) 128–140.
[56] E. Kuhl, A. Menzel, P. Steinmann, Computational modeling of growth, Comput. Mech. 32 (1–2) (2003) 71–88.
[57] E. Kuhl, P. Steinmann, Theory and numerics of geometrically nonlinear open system mechanics, Internat. J. Numer. Methods Engrg. 58 (11) (2003) 1593–1615.
[58] P. Saez, E. Pena, J.M. Tarbell, M.A. Martinez, Computational model of collagen turnover in carotid arteries during hypertension, Internat. J. Numer. Methods Engrg. 31 (2) (2015).
[59] E.K. Rodriguez, A. Hoger, A.D. McCulloch, Stress-dependent finite growth in soft elastic tissues, J. Biomech. 27 (1994) 455–467.
[60] K.E. Murphy, S.W. McCue, DLS. McElwain, Clinical strategies for the alleviation of contractures from a predictive mathematical model of dermal repair, Wound Repair Regen 20 (2012) 194–202.
[61] T.C. Gasser, R.W. Ogden, G.A. Holzapfel, Hyperelastic modelling of arterial layers with distributed collagen fibre orientations, J. R. Soc. Interface 3 (6) (2006) 15–35.
[62] A. Menzel, M. Harrysson, M. Ristinmaa, Towards an orientation-distribution-based multi-scale approach for remodelling biological tissues, Comput. Methods Biomech. Biomed. Eng. 11 (5) (2008) 505–524.
[63] P. Saez, A. Garcia, E. Pea, T.C. Gasser, M.A. Martinez, Microstructural quantification of collagen fiber orientations and its integration in constitutive modeling of the porcine carotid artery, Acta Biomater. 33 (2016) 183–193.
[64] D.H. Cortes, S.P. Lake, J.A. Kadlowec, L.J. Soslowsky, D.M. Elliott, Characterizing the mechanical contribution of fiber angular distribution in connective tissue: comparison of two modeling approaches, Biomed. Model. Mechanobiol. 9 (2010) 651–658.
[65] V. Alastrue, M.A. Martinez, M. Doblare, A. Menzel, Anisotropic micro-sphere-based finite elasticity applied to blood vessel modelling, J. Mech. Phys. Solids 57 (1) (2009) 178–203.
[66] A. Menzel, T. Waffenschmidt, A microsphere-based remodelling formulation for anisotropic biological tissues, Phil. Trans. R. Soc. A 367 (1902) 3499–3523.

[67] A. Buganza Tepole, H. Kabaria, K.U. Bletzinger, E. Kuhl, Isogeometric Kirchhoff–Love shell formulations for biological membranes, Comput. Methods Appl. Mech. Engrg. 293 (2015) 328–347.
[68] S. Roy, S. Biswas, S. Khanna, G. Gordillo, V. Bergdall, J. Green, C.B. Marsh, L.J. Gould, CK. Sen, Characterization of a preclinical model of chronic ischemic wound, Physiol. Genom 37 (3) (2009) 211–224.
[69] V. Saxena, C.W. Hwang, S. Huang, Q. Eichbaum, D. Ingber, D.P. Orgill, Vacuum-assisted closure: microdeformations of wounds and cell proliferation, Plast. Reconstr. Surg. 114 (5) (2004) 1086–1096.
[70] N.J.B. Driessen, G.W.M. Peters, J.M. Huyghe, C.V.C. Bouten, FPT. Baaijens, Remodelling of continuously distributed collagen fibers in soft connective tissues, J. Biomech. 36 (2003) 1151–1158.
[71] G. Himpel, A. Menzel, E. Kuhl, P. Steinmann, Time-dependent fibre reorientation of transversely isotropic continua - Finite element formulation and consistent linearization, Internat. J. Numer. Methods Engrg. 73 (2008) 1413–1433.
[72] T. Hillen, K. Painter, A user's guide to PDE models for chemotaxis, J. Theoret. Biol. 58 (2008) 183–217.
[73] A. Besser, U.S. Schwarz, Coupling biochemistry and mechanics in cell adhesion: a model for inhomogeneous stress fiber contraction, New J. Phys. 9 (11) (2007) 425.
[74] L. Olsen, J.A. Sherratt, P.K. Maini, A mechanochemical model for adult dermal wound contraction and the permanence of the contracted tissue displacement profile, J. Theoret. Biol. 177 (2) (1995) 113–128.
[75] P. Moreo, J.M. Garcia-Aznar, M. Doblare, Modeling mechanosensing and its effect on the migration and proliferation of adherent cells, Acta Biomater. 4 (3) (2008) 613–621.
[76] H. Hu, F. Sachs, Stretch-activated ion channels in the heart, J. Mol. Cell Cardiol. 29 (6) (1997) 1511–1523.
[77] I.B. Bischofs, U.S. Schwarz, Cell organization in soft media due to active mechanosensing, Proc. Natl. Acad. Sci. USA 100 (16) (2003) 9274–9279.
[78] H.M. Powell, K.L. McFarland, D.L. Butler, D.M. Supp, ST. Boyce, Uniaxial strain regulates morphogenesis, gene expression, and tissue strength in engineered skin, Tissue Eng. A 16 (3) (2010) 1083–1092.
[79] D. Kessler, S. Dethlefsen, I. Haase, M. Plomann, F. Hirche, T. Krieg, B. Eckes, Fibroblasts in mechanically stressed collagen lattices assume a "synthetic" phenotype, J. Biol. Chem. 276 (39) (2001) 36575–36585.
[80] C. Obbink-Huizer, C.W. Oomens, S. Loerakker, J. Foolen, C.V. Bouten, FP. Baaijens, Computational model predicts cell orientation in response to a range of mechanical stimuli, Biomech. Model. Mechanobiol. 13 (1) (2014) 227–236.
[81] N.J. Driessen, M.A. Cox, C.V. Bouten, F.P. Baaijens, Remodelling of the angular collagen fiber distribution in cardiovascular tissues, Biomech. Model. Mechanobiol. 7 (2) (2008) 93–103.
[82] B.A. Schmidt, V. Horsley, Intradermal adipocytes mediate fibroblast recruitment during skin wound healing, Development 140 (2013) 1517–1527.
[83] J. Massague, The transforming growth factor-beta family, Ann. Rev. Cell Biol. 6 (1) (1990) 597–641.
[84] L.E. Bowes, M.C. Jimenez, E.D. Hiester, M.S. Sacks, J. Brahmatewari, P. Mertz, W.H. Eaglstein, Collagen fiber orientation as quantified by small angle light scattering in wounds treated with transforming growth factor $\beta 2$ and its neutralizing antibody, Wound Repair Regen 7 (3) (1999) 179–186.
[85] B.D. Cumming, D.L.S. McElwain, Z. Upton, A mathematical model of wound healing and subsequent scarring, J. R. Soc. Interface 7 (2009) 19–34.
[86] G.E. Lindahl, R.C. Chambers, J. Papakrivopoulou, S.J. Dawson, M.C. Jacobsen, J.E. Bishop, G.J. Laurent, Activation of fibroblast procollagen alpha 1(I) transcription by mechanical strain is transforming growth factor-beta-dependent and involves increased binding of CCAAT binding factor (CBF/NF-Y) at the proximal promoter, J. Biol. Chem. 277 (8) (2002) 6153–6161.
[87] A. Fine, R.H. Goldstein, The effect of transforming growth factor-beta on cell proliferation and collagen formation by lung fibroblasts, J. Biol. Chem. 262 (1987) 3897–3902.
[88] H.R. Chaudhry, Optimal patterns for suturing wounds, J. Biomech. 31 (7) (1998) 653–662.
[89] C.W. Berard, S.C. Woodward, J.B. Herrmann, EJ. Pulaski, Healing of incisional wounds in rats the relationship of tensile strength and morphology to the normal skin wrinkle lines, Ann. Surg. 159 (2) (1964) 260.
[90] A. Buganza Tepole, M. Gart, C.A. Purnell, A.K. Gosain, E. Kuhl, The incompatibility of living systems: Characterizing growth-induced incompatibilities in expanded skin, Ann. Biomed. Eng. (2015) 1–19.
[91] F.H. Silver, L.M. Siperko, G.P. Seehra, Mechanobiology of force transduction in dermal tissue, Skin Res. Tech. 9 (2003) 3–23.
[92] T.A. Peterson, E. Doughty, M.G. Kann, Towards precision medicine: advances in computational approaches for the analysis of human variants, J. Mol. Biol. 425 (21) (2013) 4047–4063.
[93] H.P. Ehrlich, Wound closure: evidence of cooperation between fibroblasts and collagen matrix, Eye 2 (1988) 149–157.
[94] L. Cooper, C. Johnson, F. Burslem, P. Martin, Wound healing and inflammation genes revealed by array analysis of macrophageless PU. 1 null mice, Genome Biol. 6 (1) (2004) R5.
[95] G.J. Laurent, Dynamic state of collagen: pathways of collagen degradation in vivo and their possible role in regulation of collagen mass, Am. J. Physiol. Cell. Physiol. 252 (1987) 1–9.
[96] A. Buganza Tepole, C.J. Ploch, J. Wong, A.K. Gosain, E. Kuhl, Growing skin—A computational model for skin expansion in reconstructive surgery, J. Mech. Phys. Solids 59 (2011) 2177–2190.
[97] M.S. Kolodney, R.B. Wysolmerski, Isometric contraction by fibroblasts and endothelial cells in tissue culture: a quantitative study, J. Cell Biol. 117 (1) (1992) 73–82.
[98] C. Valero, E. Javierre, J.M. Garcia-Aznar, M.J. Gómez-Benito, A cell-regulatory mechanism involving feedback between contraction and tissue formation guides wound healing progression, PLoS One 9 (3) (2014) e92774. http://dx.doi.org/10.1371/journal.pone.0092774.
[99] J.G. Goodhill, Diffusion in axon guidance, Eur. J. Neurosci. 9 (1997) 1414–1412.